22. Moiré Interferometry

D. Post, B. Han

The basic concepts and practice of moiré interferometry are reviewed. Moiré interferometry provides contour maps of in-plane displacement fields with high sensitivity and high spatial resolution. It has matured as an invaluable tool for engineering analyses, proved by many industrial and scientific applications. With the typical reference grating frequency of 2400 lines/mm, the contour interval is 0.417 μm displacement per fringe order. For microscopic moiré interferometry, sensitivity in the nanometer range has been achieved. Reliable normal strains and shear strains are extracted from the displacement data for bodies under mechanical, thermal and environmental loading.

22.1 **Current Practice** 4
22.1.1 Specimen Gratings 4
22.1.2 Optical Systems 6
22.1.3 The Equations 6
22.1.4 Fringe Counting 7
22.1.5 Strain Analysis 8
22.2 **Important Concepts** 8
22.2.1 Physical Description 8
22.2.2 Theoretical Limit 9
22.2.3 Black Holes 9
22.2.4 Insensitive to Out-of-Plane Deformation 9
22.2.5 Accidental Rigid Body Rotation 11
22.2.6 Carrier Fringes 11
22.2.7 Loading: Mechanical, Thermal, etc. 11
22.2.8 Bithermal Loading 12
22.2.9 Curved Surfaces 14
22.2.10 Data Enhancement/Phase Stepping 14
22.2.11 Microscopic Moiré Interferometry 17
22.3 **Challenges** 18
22.3.1 Strain Analysis 18
22.3.2 Replication of Deformed Gratings ... 18
22.4 **Characterization of Moiré Interferometry** . 19
22.5 **Moiré Interferometry in the Microelectronics Industry** 19
22.5.1 Temperature-Dependent Deformation 20
22.5.2 Hygroscopic Deformation 20
22.5.3 Standard Qualification Test of Optoelectronics Package 22
22.5.4 Micromechanics Studies by Microscopic Moiré Interferometry ... 25
References 26

This section introduces basic concepts of moiré interferometry and their evolution, leading to the current practice. Moiré interferometry has become an important tool in industrial, research and academic organizations. The tool is used to measure tiny deformations of solid bodies, caused by mechanical forces, temperature changes, or other environmental changes. It is the in-plane deformations that are measured, namely the U and V components of displacement that are parallel to the surface of the body. These are the displacements from which the induced strains and stresses are determined.

Moiré interferometry has been applied for studies of composite materials, polycrystalline materials, layered materials, piezoelectric materials, fracture mechanics, biomechanics, structural elements, and structural joints. It is practiced extensively in the microelectronics industry to measure thermally induced deformation of electronic packages.

For in-plane displacement measurements, the technology has evolved beautifully from low-sensitivity geometric moiré to the powerful capabilities of moiré interferometry. Moiré measurements are performed routinely in the interferometric domain with fringes

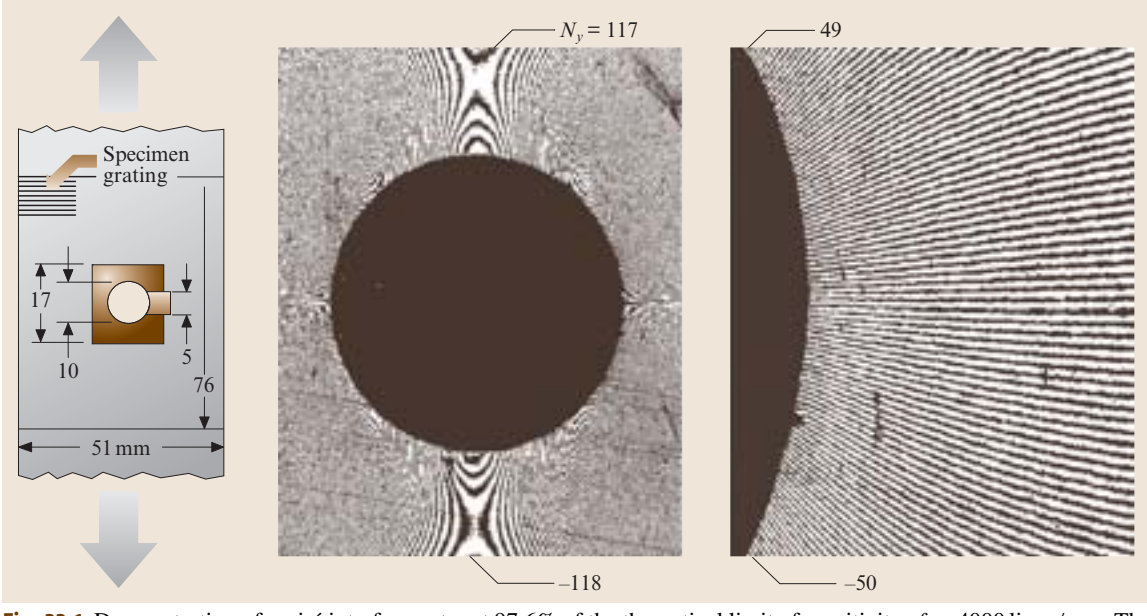

Fig. 22.1 Demonstration of moiré interferometry at 97.6% of the theoretical limit of sensitivity. $f = 4000$ lines/mm. The patterns are from the shaded regions. Excellent fringe resolution was evident in the full 76×51 mm specimen grating area

representing subwavelength displacements per contour. Since moiré responds only to geometric changes, it is equally effective for elastic, viscoelastic, and plastic deformations, for isotropic, orthotropic and anisotropic materials, and for mechanical, thermal, and dynamic loadings.

The history of moiré interferometry is described in [22.1]; in that paper, "A Historical Review of Moiré Interferometry," *Walker* recounted the pioneering developments in Japan, which predated accomplishments in the Western world by several years, but was not widely known in the West. He outlined work by Sciamarella and by Post and their students in the U.S., and by several investigators in Europe – especially the outstanding work at Strathclyde University by McKelvie, Walker and their colleagues. Moiré interferometry has matured through worldwide efforts.

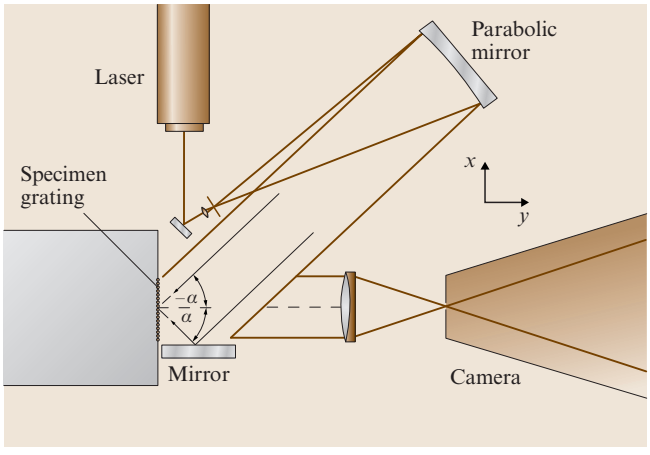

Fig. 22.2 Optical system for Fig. 22.1: Lloyd's mirror arrangement

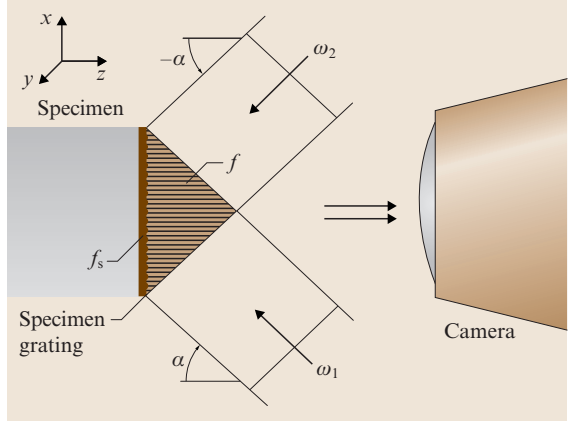

Fig. 22.3 The deformed specimen grating interacts with the virtual reference grating to form the moiré pattern. The phenomenon is analogous to geometric moiré

Work at Virginia Tech began in 1979, where we were responsible for numerous advances. We felt confidence in the power of the method in 1981 when *Weissman* [22.2] produced the fringe pattern shown in Fig. 22.1. It depicts the vertical displacement field surrounding a hole in a plate loaded in tension. It demonstrated the moiré effect at 4000 lines/mm. It demonstrated moiré interferometry at 97.6% of its theoretical limit of sensitivity. It demonstrated the V deformation field with a huge number of fringes, or displacement contours, and the fringes had superb visibility.

The instrumentation was simple, as illustrated in Fig. 22.2. A phase grating of 2000 lines/mm was formed on the specimen, and it deformed together with the specimen as the specimen was loaded. A Lloyd's mirror arrangement created a 4000 lines/mm interference fringe pattern in the same space, and that pattern acted as the reference grating. It is called a *virtual* reference grating. (It was not a *real* reference grating of the sort used in geometric moiré, but instead, it was an interference pattern formed in space that functioned as a reference grating.) The specimen grating and the reference grating interacted to form the moiré fringes of Fig. 22.1. The scheme is illustrated in Fig. 22.3, where the two coherent beams from the Lloyd's mirror arrangement interfere to form the virtual reference grating of frequency f, which interacts with the specimen grating of frequency f_s to create the moiré pattern.

Stepping back, the transition from geometric moiré to moiré interferometry evolved largely in the 1970s. Whereas only low frequency gratings could be applied to specimens, high frequency reference gratings could be used, together with an optical filtering arrangement, to produce moiré fringe multiplication. The fringe multiplication factor, β, was the ratio of grating frequencies, and the sensitivity corresponded to the pitch of the high frequency reference grating; the sensitivity became β times that of standard geometric moiré, where specimen and reference gratings of equal frequencies are used. Multiplication by $\beta = 60$ was documented [22.3], but at a substantial sacrifice of the efficiency of light utilization.

Then it was realized that light diffracted by a real reference grating (BB) creates a virtual reference grating, as illustrated in Fig. 22.4a. It is the virtual grating that interacts with the specimen grating to create the moiré pattern. Consequently, it was realized that the interference pattern produced by the intersection of any two mutually coherent beams (Fig. 22.4b) can act as

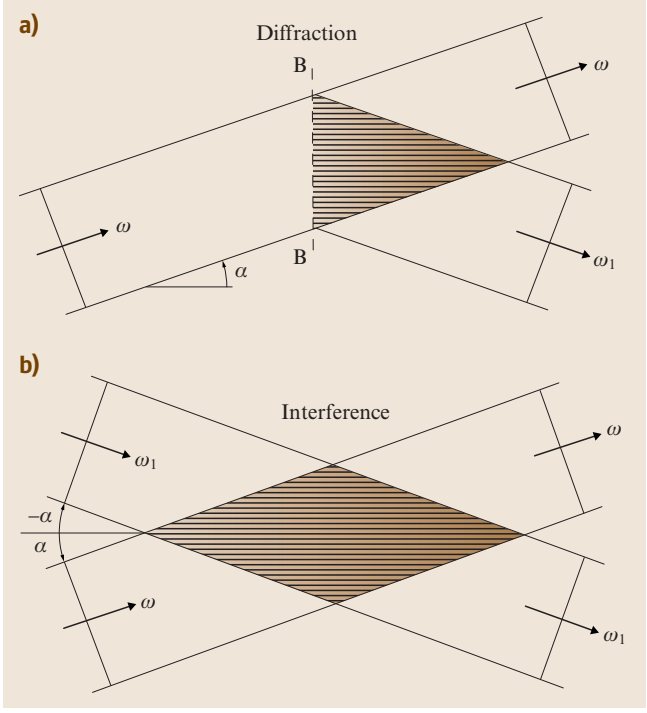

Fig. 22.4a,b Virtual gratings formed (**a**) by a real grating, and (**b**) by two coherent beams

a virtual reference grating and it can replace the real reference grating. Thus, in Fig. 22.2 the direct and the reflected beams, intersecting at angle 2α, provided the virtual reference grating.

(An important equivalency principle is acting here: interference of two beams creates a virtual grating of frequency f; a real grating of frequency f creates the same two beams [22.4]. In fact, this equivalency is also the basis of holography.)

It became clear that phase gratings (ridges and furrows) could be used as well as the amplitude gratings (bars and spaces) of geometric moiré. Several innovations evolved to link the techniques of the 1970s to the present. A significant factor was the practical availability of the laser, which provided very high monochromatic purity and allowed high contrast two-beam optical interference even when the beams traveled substantially unequal path lengths. The laser led to a practical technique to produce high frequency phase-type specimen gratings.

For this process, a setup with a beam-splitter and mirrors formed the two mutually coherent beams of Fig. 22.4b. A plate with a photosensitive coating – pho-

tographic emulsion or photoresist – was inserted to record the virtual grating. When developed, the plate exhibited the ridges and furrows of a phase grating, in exact registration with the bands of constructive and destructive interference of the virtual grating. Subsequently, the phase grating was replicated on the specimen by known techniques, using silicone rubber, epoxy, or various plastics to reproduce the array of ridges and furrows on the specimen.

Specimen gratings of very high frequency could be made, so the need for high fringe multiplication factors vanished. The moiré interferometry technique described here is actually moiré fringe multiplication with a multiplication factor of two. It utilizes the first-order diffractions from the specimen grating instead of high diffraction orders. The choice circumvents the inefficient light utilization and increased optical noise associated with higher orders, while maintaining the advantage of viewing the specimen at normal incidence.

Numerous refinements were introduced in the 1980s. Cross-line specimen gratings, together with 4-beam moiré interferometers became standard practice; this eliminated the classical uncertainty of shear measurements and enabled accurate determination of both shear and normal strains. The use of carrier fringes became common. Practical techniques for measurement of thermal strains were developed. Achromatic moiré interferometers were developed. Microscopic moiré interferometry was introduced.

In the 1990s, CCD cameras became popular for recording the fringe patterns. This led to phase stepping and automated full-field strain maps. Phase stepping proved to be an important asset for cases where fringes were sparse, because phase stepping increases the quantity of data for analysis. (For typical applications, where the fringe data is abundant, phase stepping is superfluous and sometimes counterproductive.)

A very important milestone occurred in the 1990s. IBM Corporation discovered the value of moiré interferometry for experimental analysis of thermal deformation of microelectronic devices. It was used to measure – sometimes to discover – the deformation behavior of their small complex structures, and to guide and verify their numerical analyses. Since then, moiré interferometry has propagated extensively in the electronic packaging industry, to become a standard tool for experimental analysis.

Item 1 in the Bibliography provides comprehensive coverage of the theory and practice, and diverse applications of moiré interferometry in one volume. The present chapter is intended to review the basic concepts and qualities in lesser detail, but sufficient for understanding the practice and for recognizing the power and place of moiré interferometry as a tool of experimental solid mechanics.

22.1 Current Practice

Moiré interferometry was developed to measure the in-plane displacements of essentially flat surfaces. If demanded, it can cope with curved surfaces, but with greater effort; Fig. 22.15, to be addressed later, is an example.

Two displacement fields fully define the state of engineering strain along the surface. Normally two orthogonal displacement fields are recorded: the U and V fields. They represent x- and y-components of displacement at every point in the field. The data are received as moiré fringe patterns, where the fringes are contours of constant U or V displacements. Fringe orders are given the symbols N_x and N_y, where $N_x = fU$ and $N_y = fV$. The fringe orders are proportional to the displacements, and the constant of proportionality is the frequency, f, of the (virtual) reference grating. Of course, we can write the relationships in terms of the pitch g of the reference grating, since $f = 1/g$.

22.1.1 Specimen Gratings

Typically, the virtual reference grating frequency is $f = 2400$ lines/mm (60 960 lines/in); the moiré interferometer projects this grating onto the specimen. The specimen grating is a cross-line phase grating with 1200 lines/mm in both the x- and y-directions. It is usually formed on the specimen by replication from a mold, which is itself a cross-line grating. A greatly enlarged view is shown in Fig. 22.5a, illustrating the orthogonal array of hills that comprise the cross-line grating.

The replication method of Fig. 22.5b is used for diverse applications that involve larger regions of interest, e.g., larger than one square cm. The mold is prepared with a reflective metallic film, usually evaporated aluminium. A liquid adhesive, usually an epoxy, is squeezed into a thin layer between the specimen and mold. They are separated when the adhesive solidifies.

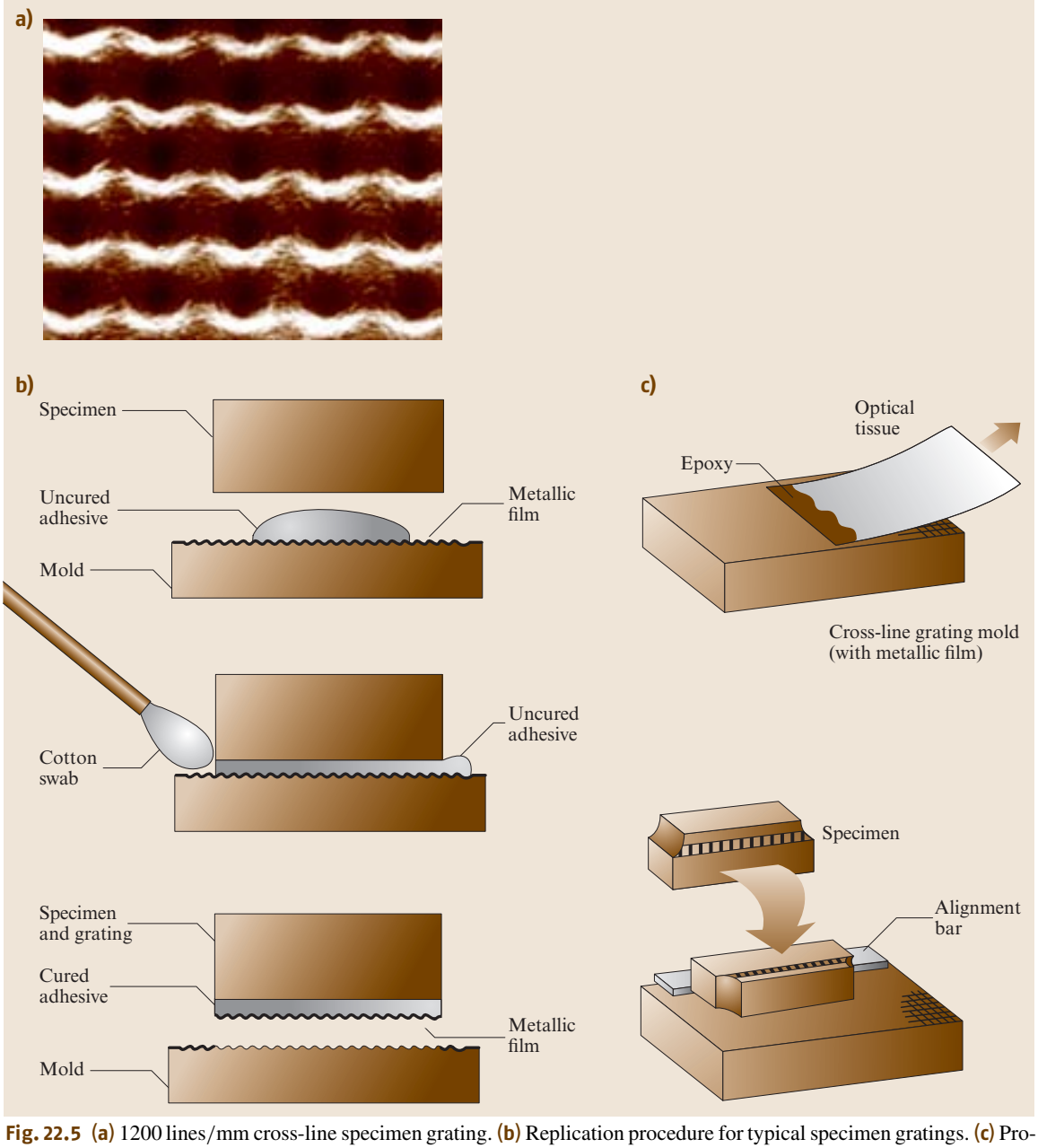

Fig. 22.5 **(a)** 1200 lines/mm cross-line specimen grating. **(b)** Replication procedure for typical specimen gratings. **(c)** Procedure for small specimens of complex geometry

The weakest interface is between the metallic film and the underlying mold, so the reflective metallic film is transferred to the specimen together with the hills and valleys of the grating. The total grating thickness is usually about 25 μm.

The technique of Fig. 22.5c is used for small specimens of complex geometry, like those encountered in electronic packaging tests. In this case, the specimen is prepared with a smooth, flat surface. A very thin layer of low viscosity adhesive is spread on the mold by the

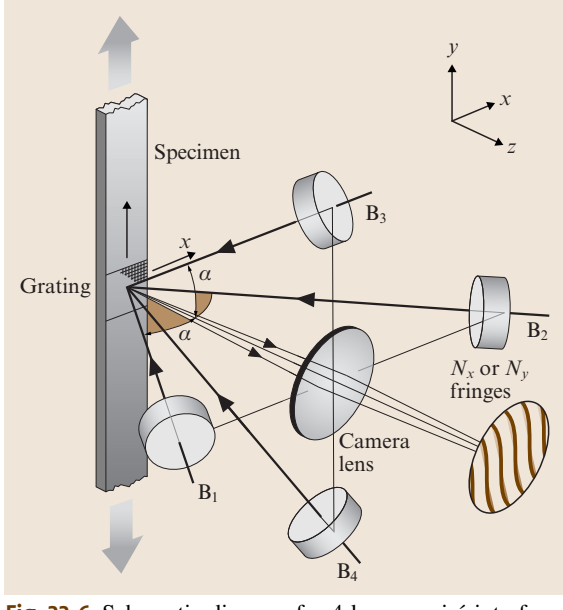

Fig. 22.6 Schematic diagram for 4-beam moiré interferometry

drag method and the specimen is pressed into the adhesive. Surface tension draws the thin adhesive away from the edges of the specimen; therefore, no cleaning operation is required to remove the excess adhesive. With this procedure, the grating thickness is usually about 2 μm. Again, the result is a thin, compliant, reflective cross-line grating, which deforms together with the underlying specimen.

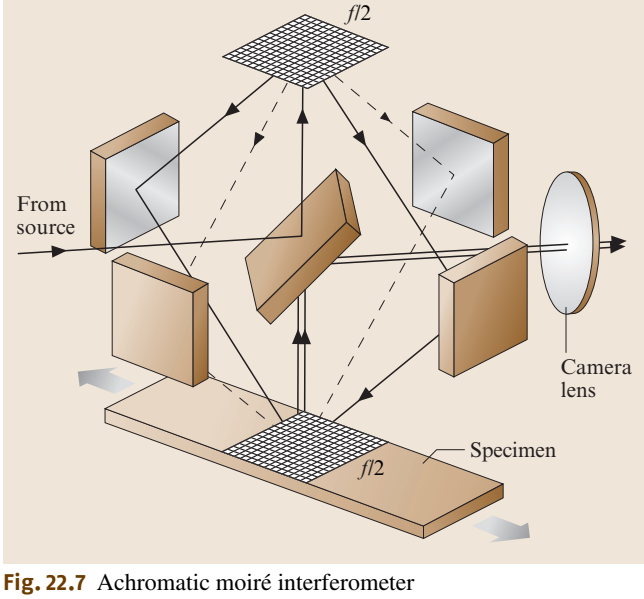

Fig. 22.7 Achromatic moiré interferometer

22.1.2 Optical Systems

The generic optical system is illustrated in Fig. 22.6. As in Fig. 22.3, two coherent, collimated beams marked B_1 and B_2 create a virtual reference grating with its lines perpendicular to the x-direction. They interact with the corresponding array of lines on the specimen grating to create the N_x fringe pattern, depicting the x-component of displacement. The fringe pattern is recorded by the camera, which is focused on the specimen. Typically, it is a digital CCD camera. Then beams B_3 and B_4 are used to record the N_y pattern. The virtual reference grating frequency is usually 2400 lines/mm. For light in the visible wavelength range, α is near 45°. The contour interval for the fringe pattern is $1/f$, i. e., a displacement of 0.417 μm per fringe order.

Numerous different optical systems can be designed to provide the essential elements of Fig. 22.6. A few systems are illustrated in [22.4]. Two-beam systems have been used for special applications. For strain and stress analysis, the 4-beam optical system offers a vital advantage: shear strains can be extracted with the same accuracy as normal strains.

Achromatic optical systems have also been devised, and Fig. 22.7 is an example [22.4]. A temporally incoherent light source can be used. With this arrangement, the angle of diffraction, α, at the upper grating changes in exact harmony with the wavelength λ to maintain a fixed frequency f of the virtual reference grating. The upper grating is called a *compensator* grating, since it compensates for variations of the wavelength. Whereas monochromatic purity is not needed, spatial coherence remains a requirement.

22.1.3 The Equations

The pertinent equations are these:

- For optical interference of 2 beams (Fig. 22.4b)

$$F = \frac{2}{\lambda}\sin\theta, \tag{22.1}$$

  where F is the fringe frequency (fringes/mm) in the region of intersection, λ is the wavelength, and θ is the half-angle of intersection.
- For the moiré interferometer

$$\sin\alpha = \frac{\lambda f}{2}, \quad f = 2f_s \tag{22.2}$$

where f and f_s is the frequency of the virtual reference grating and the specimen grating, respectively.

- For the displacements at each point in the field

$$U = \frac{1}{f} N_x; \quad V = \frac{1}{f} N_y, \tag{22.3}$$

where U and V are displacements in the x- and y-directions, respectively.

- For the strains at each point

$$\varepsilon_x = \frac{\partial U}{\partial x} = \frac{1}{f}\left(\frac{\partial N_x}{\partial x}\right),$$

$$\varepsilon_y = \frac{\partial V}{\partial y} = \frac{1}{f}\left(\frac{\partial N_y}{\partial y}\right), \tag{22.4}$$

$$\gamma_{xy} = \frac{\partial U}{\partial y} + \frac{\partial V}{\partial x} = \frac{1}{f}\left(\frac{\partial N_x}{\partial y} + \frac{\partial N_y}{\partial x}\right), \tag{22.5}$$

where ε and γ are normal and shear strains, respectively. Thus, the strains are determined by the rate of change of fringe orders in the patterns, or the fringe gradient surrounding each point.

- For fringe gradients

$$\frac{\partial N_x}{\partial x} \approx \frac{\Delta N_x}{\Delta x}; \text{ etc.} \tag{22.6}$$

The derivatives are usually approximated by their finite increments, i. e., the change of fringe order that occurs in a finite distance Δx.

- For the stresses

Stresses are determined from the strains, using the stress-strain relationships (or the constitutive equations) for the specimen material.

22.1.4 Fringe Counting

The rules of topography of continuous surfaces govern the order of fringes [22.5]. Fringes of unequal orders cannot intersect. The fringe order at any point is unique, independent of the path of the fringe count used to reach the point.

The location of a zero-order fringe in a moiré pattern can be selected arbitrarily. Any fringe – black, white or gray – can be assigned as the zero order fringe. This is because rigid-body translations are not important in deformation analysis. Absolute displacement information is not required and relative displacements can be determined using an arbitrary datum. In Fig. 22.8, the zero fringe is assigned in the lower left region of the specimen. Of course, at every point along this continuous fringe, $N_y = 0$.

Figure 22.8 shows the deformation of a tensile coupon cut from a stainless steel plate in the region of a weld. Cracks appear in the weld, but along the left edge of the specimen, the material is continuous. Since the strain is tensile, or positive, the fringe orders along the left edge increase monotonically in the $+y$-direction, as shown. Then the fringe orders can be assigned at every point in the field by following continuous fringes across the field. Fringe orders along the right edges were assigned accordingly.

Where a crack is present, the V displacements are different along the upper and lower lips of the crack. This accounts for the crack opening that results from the tensile load. For example, at the right edge the fringe order changes from $N_y = 3$ to $N_y = 10$, indicating a crack-opening displacement of 7 fringe orders, or 2.9 µm (115 µin).

Clues derived from known loading conditions and known specimen geometry are often sufficient to establish the sign of the fringe gradient at every point, i. e., to establish whether the fringe order is increasing or decreasing as the count progresses from one fringe to the neighboring fringe. Occasionally the clues might not be sufficient, but there is always a simple experimental way to determine the sign of the fringe gradient.

If during the experiment, the specimen is moved gently in the $+x$-direction, the fringe order N_x at every point increases. This means that the fringes all move to-

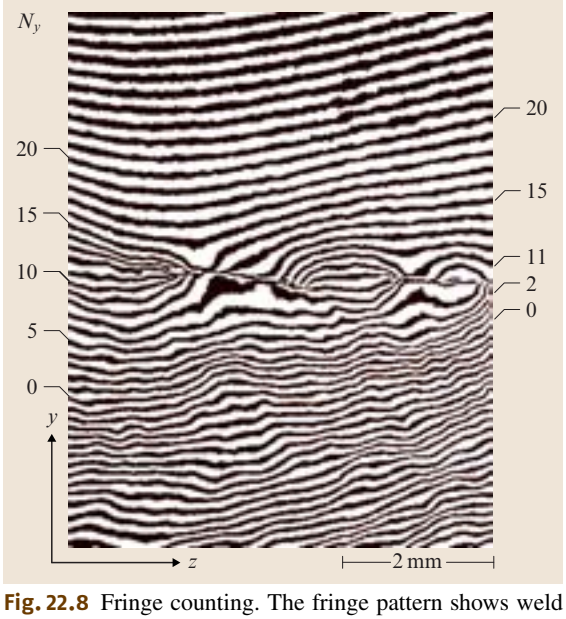

Fig. 22.8 Fringe counting. The fringe pattern shows weld defects in a stainless steel tension specimen. f = 2400 lines/mm. (Courtesy of S. A. Chavez)

ward the direction of *lower-order fringes.* Thus, if the N_x fringes move in the negative x-direction, the gradient $\partial N_x/\partial x$ is positive. The argument is the same for the y-direction. A convenient alternative is available if the moiré interferometer is equipped for phase stepping (fringe shifting). The investigator can watch the pattern while the fringes are shifted. Again, the fringes move toward lower fringe orders when the phase is increased. Thus, the sign of the fringe gradients is readily determined at any point.

22.1.5 Strain Analysis

Strains are determined from the two displacement fields by the relationships for engineering strain, (22.4) and (22.5). In principle, the exact differential can be extracted at any point by plotting a curve of fringe orders along a line through the point and measuring the slope of the curve at the point. Often, however, the finite increment approximation is sufficient, whereby (as an example) $\partial N_x/\partial x$ is taken to be equal to $\Delta N_x/\Delta x$. In that case, strain is determined by measuring Δx, the distance between neighboring fringes, in the immediate neighborhood of the point of interest.

Shear strains are determined as readily as normal strains. Numerous examples of fringe counting and strain analysis are given in [22.4]. In nearly all cases of strain analysis, the strains are sought at specific points (e.g., where the fringes are most closely spaced, indicating strain maxima), or along specific lines. Manual methods, and computer-assisted methods are most practical for such cases.

22.2 Important Concepts

22.2.1 Physical Description

The description offered with Fig. 22.3 is a casual explanation based upon the analogy to geometric moiré. Nevertheless, it is effective. The rigorous analysis of moiré interferometry [22.4], based on diffraction and optical interference, shows that the fringe order/displacement relationship is identical for moiré interferometry and geometric moiré. The simple, intuitive procedures to extract data from geometric moiré patterns apply also to moiré interferometry patterns. This is important for our colleagues who might practice moiré interferometry, but specialize in diverse aspects of engineering and materials science, as distinct from specialists in optical techniques.

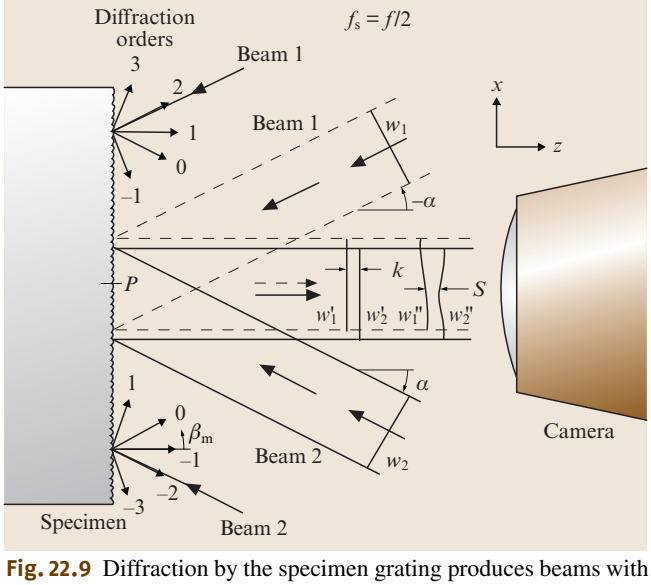

Fig. 22.9 Diffraction by the specimen grating produces beams with plane wave fronts for the no-load condition. Warped wave fronts result from inhomogeneous deformation of the specimen

For our colleagues in photomechanics, the physical description illustrated in Fig. 22.9 is more satisfying. Before loads are applied to the specimen, the grating on its surface has a uniform frequency of f_s. The incident beam 1 is diffracted such that its first order emerges normal to the specimen, with wave front w_1'. This requires that $\sin\alpha = \lambda f_s$. Similarly, beam 2 is diffracted to form emergent wave front w_2'. For these initial conditions, the emergent beams have parallel wave fronts and they interfere to create a null field, i. e., a uniform intensity or the infinite fringe.

Incidentally, we note from (22.1) that when two beams intersect with this half-angle α, they generate interference fringes of frequency f, where $f \equiv 2f_s$. Thus, the frequency of the virtual reference grating of Fig. 22.3 is twice the initial frequency of the specimen grating. This is the condition that provides normal viewing, without distortion of the image.

For a complex specimen, the specimen grating deforms nonuniformly when loads are applied. The grating pitch and orientation vary as continuous functions along the specimen. Consequently the directions of diffracted rays change continuously, and the two beams emerge as warped wave fronts w_1'' and w_2''. They

interfere to generate contours of their separation S, and this interference pattern is recorded by the camera. With the camera focused on the plane of the specimen, the image is the moiré pattern – the map that depicts the in-plane deformation of the specimen. Summing up, moiré interferometry is a case of two-beam interferometry.

It is important to focus the camera on the plane of the specimen. Since wave front warpage changes as the wave travels away from the specimen, it is especially important for cases of strong strain gradients and the concomitant strong warpage of the emerging wave fronts. The issue is addressed in [22.4].

22.2.2 Theoretical Limit

From (22.2), we see that the theoretical upper limit for the reference grating frequency is approached as α (Fig. 22.6) approaches 90°. The theoretical limit is $f = 2/\lambda$. The corresponding theoretical upper limit of sensitivity is $2/\lambda$ fringes per unit displacement, which corresponds to a contour interval of $\lambda/2$ displacement per fringe order.

In the experiment of Fig. 22.1, α was 77.4° and λ was 488.0 nm. This produced a virtual reference grating of 4000 lines/mm (101 600 lines/in). For this wavelength, the theoretical limit is $f = 4098$ lines/mm, which means that the experiment was conducted at 97.6% of the theoretical limit of sensitivity.

The theoretical limit pertains to virtual reference gratings formed in air. In the experimental arrangement described later for microscopic moiré interferometry, the grating is formed in a refractive medium.

22.2.3 Black Holes

Referring to Fig. 22.9, we can visualize that the angles of diffraction from any region of the specimen stems from two effects: (1) the load-induced strain and (2) the load-induced surface slope. If the angles of diffraction become large enough, light from that region can miss the lens and never enter the camera. The region appears black in the image – it is called a *black hole*.

In such cases, the main cause is usually the surface slope. It is rare that a homogeneous body would exhibit large slopes. A composite body, fabricated by joining two dissimilar materials, can exhibit large slopes near the interface as a result of a Poisson's ratio mismatch. Experience indicates that the slopes are seldom severe enough to cause black regions until very high strain levels are reached.

The camera lens can be translated laterally to capture the light of the moiré pattern that is otherwise lost. In doing so, it is possible that other regions will become black. An alternative is to replace the camera lens with a lens of larger numerical aperture, and this might necessitate viewing the specimen at higher magnification.

22.2.4 Insensitive to Out-of-Plane Deformation

This is largely a pedagogical issue, inasmuch as the literature may not be sufficiently clear. Various publications show sensitivity to out-of-plane rotations. However, the rigorous mathematical analysis of [22.4] proves that moiré interferometry is insensitive to all out-of-plane motions, including rotations. Where do the publications deviate?

Figure 22.10 should help clarify the issue. It represents the planes, or *walls of interference* of the virtual reference grating, and it also represents the plane of the undeformed specimen grating as plane *abcd*. Let P be a point fixed on the specimen grating, and let P move to another point in space, P′, when the specimen is deformed. The deformed surface surrounding P′ might have any slope, as indicated by the dashed box. As the point moves in the x-direction, it cuts through walls of interference and therefore causes a change of fringe order in the moiré pattern. Expressed in other words, the point crosses lines of the (virtual) reference grating. For displacement components V and W, the point does not cross any wall, and therefore these com-

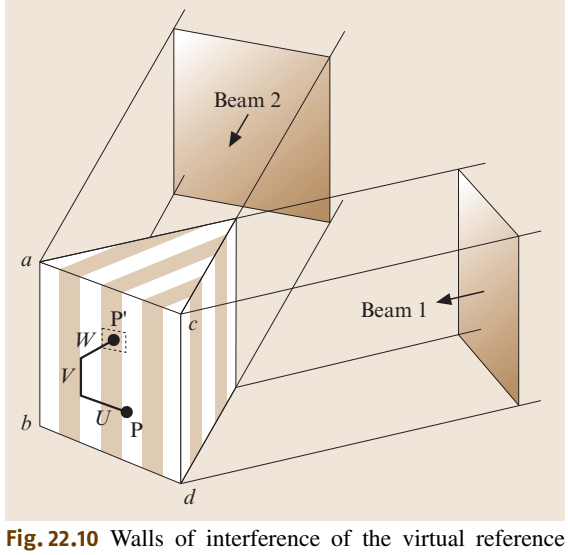

Fig. 22.10 Walls of interference of the virtual reference grating. Only the U component of displacement crosses the walls of the reference grating

ponents have no effect on the fringe order. The moiré pattern remains insensitive to V and W regardless of the surface slope. This corroborates the proof that moiré interferometry senses only the component of displacement perpendicular to the walls of the virtual reference grating.

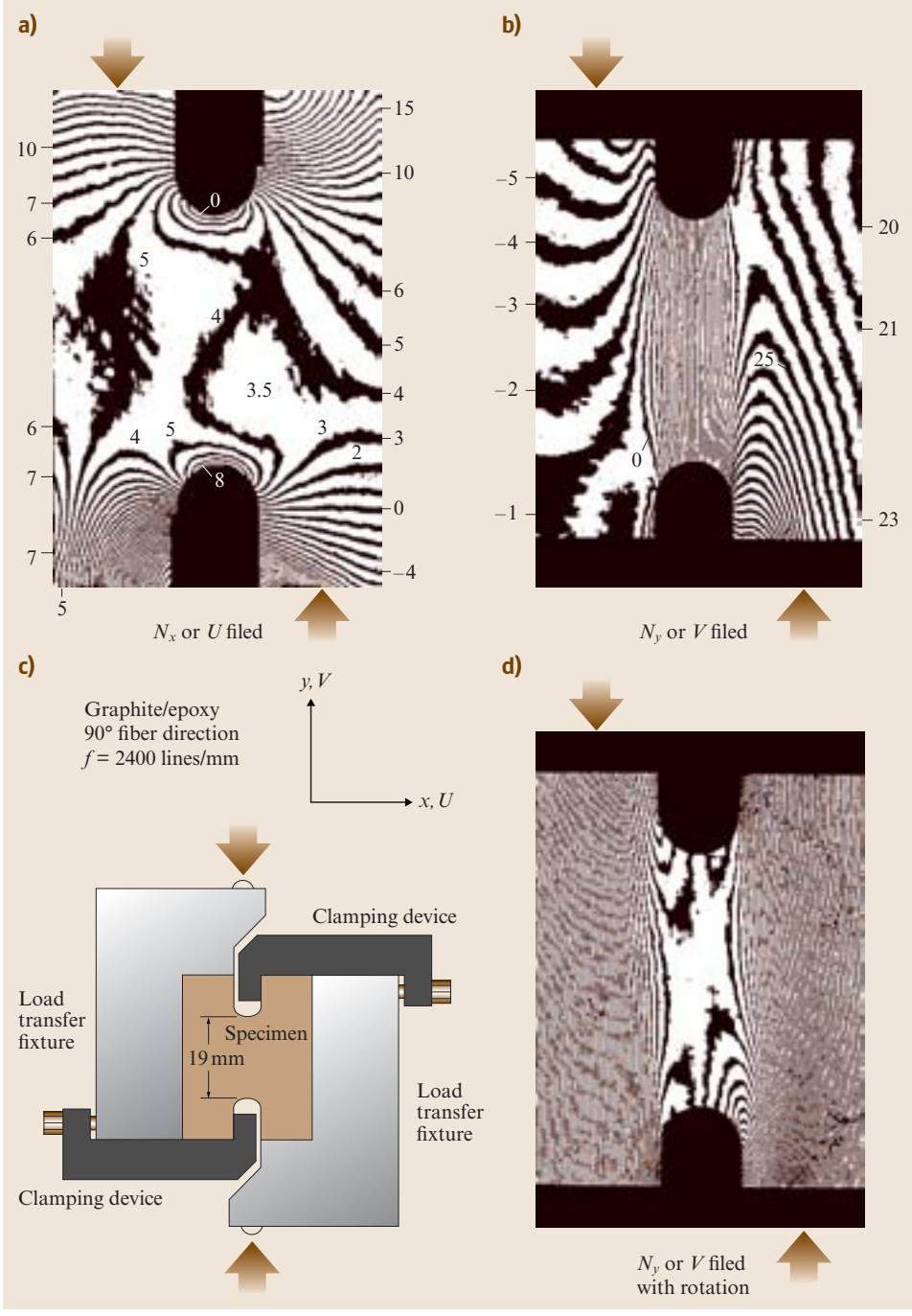

Fig. 22.11 Displacement fields for a compact shear specimen. Carrier fringes of rotation transform the V field. Local irregularities in the fringes are caused by local variations in the composite material. (Courtesy of P. G. Ifju)

Engineering strain is the ratio of the local change of length to the original length, when both are projected onto the original specimen surface *abcd*. Thus, engineering strains are correctly determined by (22.4) and (22.5), regardless of surface slopes. Note that out-of-plane displacements are referenced to the original surface, too.

For exceptional studies in which the surface slope is large enough, the investigator might be interested in these lengths measured on the specimen surface instead of plane *abcd*. This is where the publications deviate. In such cases, a mathematical transformation is required which involves additional variables, specifically the components of the surface slopes. These slopes must be measured (or otherwise determined) to augment the moiré data at each point where the strain is to be calculated. Thus, if the investigator feels the out-of-plane slopes are significant enough to degrade the accuracy that is sought for a specific analysis, then a Lagrangian strain or other three-dimensional strain should be calculated. Otherwise, the investigator accepts that the influence of the slope is negligible for calculating the strain.

Note, too, that special apparatus and procedures may be required to record an image of the moiré fringes when surface slopes become large. Otherwise, the moiré pattern may display *black holes* in regions of large slopes. In general, it is the engineering strain that is sought by moiré interferometry, not a transformed strain, and (22.4) and (22.5) are fully effective.

22.2.5 Accidental Rigid Body Rotation

The previous paragraph refers to out of-plane deformations induced by the loads – not rigid-body motions. In practice, the specimen is observed in its no-load condition and the moiré interferometer is adjusted to produce a null field, i. e., a uniform fringe order throughout the field. Then the load is applied and the displacement fields are recorded.

Sometimes, an out-of-plane rigid-body rotation is introduced accidentally in the loading process. Rotation about an axis that is perpendicular to the lines of the reference grating has no effect on the fringe pattern. Rotation by Ψ about an axis parallel to the grating lines is seen as an apparent foreshortening of the specimen grating. It introduces an extraneous fringe gradient that corresponds to an apparent compressive strain ε^{app}, where

$$\varepsilon^{\text{app}} = -\frac{\Psi^2}{2} \tag{22.7}$$

provided the rotation Ψ is not large. The superscript signifies an extraneous strain, or error. The extraneous fringe gradient is a second-order effect and it can be neglected in the usual case where it is small compared to the strain-induced fringe gradient. Otherwise, a correction can be applied [22.4].

22.2.6 Carrier Fringes

An array of uniformly spaced fringes can be produced by adjustment of the moiré interferometer and these are called *carrier fringes*. With the specimen in the no-load condition, a carrier of *extension* is produced by changing angle α (Fig. 22.6). These fringes are parallel to the lines of the reference grating, just like the fringes of a pure tensile (or compression) specimen. Carrier fringes of *rotation* are produced by a rigid-body rotation of the specimen or the interferometer, and these are perpendicular to the lines of the reference grating.

It is frequently valuable to modify the load-induced fringe patterns with carrier fringes [22.6]. Figure 22.11 is an example [22.7], where the load-induced fringes are shown in a and b. The specimen is cut from a graphite/epoxy composite material and it is loaded in a compact shear fixture c. In d, the fringes in the test section between notches are subtracted off by carrier fringes of rotation. The carrier fringes are vertical and uniformly spaced, and their gradient is opposite to that of the shear-induced fringes. What is the benefit? It shows that the normal strain ε_y is zero along the vertical center line of the specimen, that ε_y is extremely small throughout the test zone, and that the shear deformation is nearly uniform over a wide test region.

Carrier fringes can be introduced easily, typically by turning an adjusting screw in the moiré interferometer. They are used, as needed, for a variety of purposes, especially to remove ambiguities and enhance the accuracy of data reduction.

For in-plane rigid-body rotation

$$\frac{\partial N_x}{\partial y} \equiv -\frac{\partial N_y}{\partial x} \,. \tag{22.8}$$

Substitution into (22.5) shows that shear strains calculated from the moiré fringes are not affected by carrier fringes of rotation (when a 4-beam moiré interferometer is used). Also, the calculated shear strains are not affected by carrier fringes of extension. The calculated normal strains are (essentially) unaffected by carrier fringes of rotation. These conditions allow beneficial changes in the fringe patterns without altering the reliability of strain calculations.

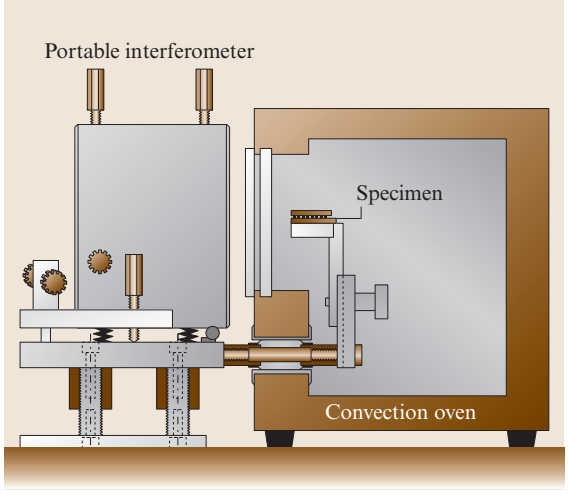

Fig. 22.12 Arrangement for real-time thermal deformation tests

22.2.7 Loading: Mechanical, Thermal, etc.

Experimental arrangements for mechanical loading are very diverse; they depend upon the size and nature of the specimen and the magnitude of the loads. In some cases it is necessary to mount the moiré interferometer on the structure of the testing machine, or to attach it to the assembly being investigated. In others, the specimen can be loaded in a fixture that rests on an optical table together with the moiré interferometer.

For real-time thermal loading, or for deformation caused by changes of moisture content, chemical activity or radioactivity, the environmental chamber must be positioned adjacent to the moiré interferometer. Figure 22.12 illustrates a scheme used for thermal deformation measurements in the electronic packaging industry. As an important factor, the specimen is connected rigidly to the interferometer. The connecting rods do not contact the chamber (only loose insulation or compliant baffles fill the air gap at the chamber wall), so vibrations in the forced air convection chamber are not transmitted to the specimen. The arrangement has proved to be very effective. It enables the recording of fringe patterns during the transition between temperature changes, during moisture ingress and egress, during chemical activity, etc. Hence, it enables real-time measurements.

Figure 22.13 is an example of real-time thermomechanical analysis of an electronic package during a thermal cycle with temperature extremes from −20 °C to 125 °C [22.8,9]. The device is an assembly of diverse materials with different coefficients of thermal expansion, so thermal stresses, strains and deformation result from any change of temperature.

The fringes are remarkably clear at this magnification, except for those in the printed circuit board (PCB) at 125 °C; the PCB is a heterogeneous material – a composite of woven glass fibers in an epoxy matrix – and because of the weave its displacement contours are very complicated. Higher magnification is indicated. Visual inspection of the V field shows opposite directions of curvature in the chip region before and after the 125 °C temperature; this behavior results from creep of the solder and molding compound. Whereas extensive computational analysis is undertaken for the mechanical design of electronic packages, the complexities of geometry and materials necessitate experimental guidance and verification.

Additional examples of moiré interferometry applied to electronic and photonic packages are shown in Sect. 22.5.

22.2.8 Bithermal Loading

Thermal deformations can also be analyzed by room temperature observations. In this technique, the specimen grating is applied at an elevated temperature, and then the specimen is allowed to cool to room temperature before it is observed in the moiré interferometer. Thus, the deformation incurred by the temperature increment is locked into the grating and recorded at room temperature.

An adhesive that cures slowly at elevated temperature is used, usually an epoxy. The specimen and mold are preheated to the application temperature; then the adhesive is applied, the mold is installed, the adhesive is allowed to cure, and the mold is removed – all at the elevated temperature. The mold is a grating on a zero-expansion substrate, so its frequency is the same at elevated and room temperatures. Otherwise, a correction is required for the thermal expansion of the mold.

These measurements can also be performed at cryogenic temperatures. In one test, the specimen grating was applied at −40 °C using an adhesive that cured in ultraviolet light.

The example shown in Fig. 22.14 is taken from an investigation of thermal stresses in a bimaterial joint [22.10]. The specimen grating was applied and cured at 157 °C and subsequently observed at 24 °C room temperature. The two materials restrained the natural contraction of each other, causing large thermal stresses and strains. The V displacement field for the 133 °C temperature increment is shown here; car-

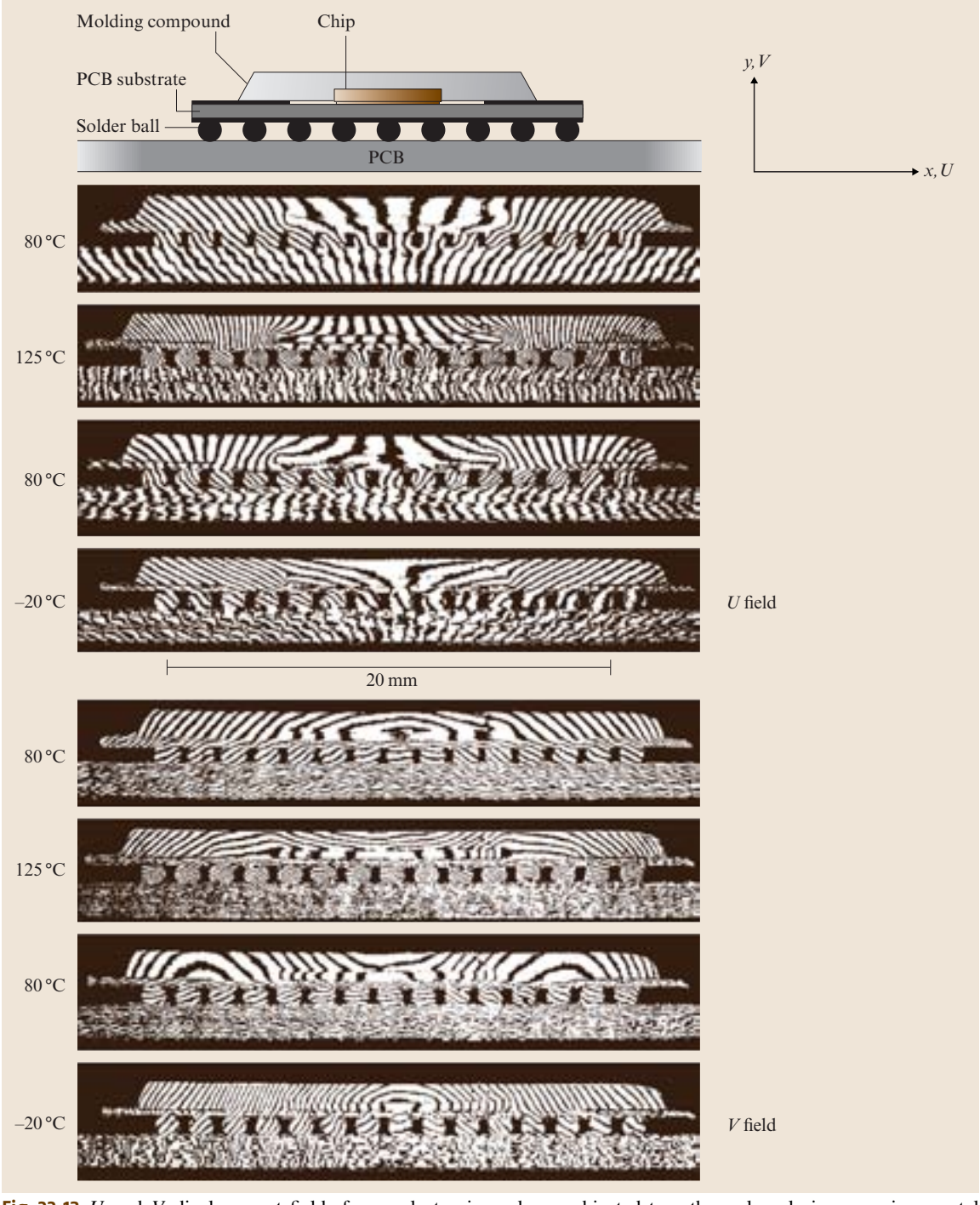

Fig. 22.13 U and V displacement fields for an electronic package subjected to a thermal cycle in an environmental chamber. $f = 2400$ lines/mm

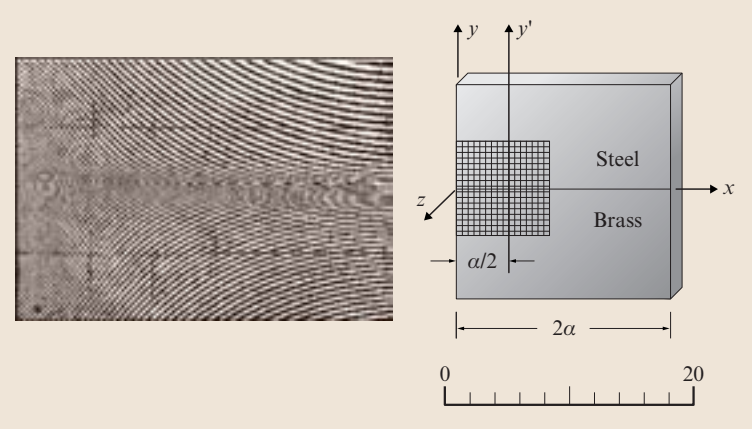

Fig. 22.14 Thermal deformation for a bimaterial joint. The N_y pattern, with carrier fringes of extension, shows the abrupt transition near the interface. $\Delta T = 133\,^{\circ}\mathrm{C}$; $a = 55.9\,\mathrm{mm}$; $f = 2400\,\mathrm{lines/mm}$. (Courtesy of J. D. Wood)

rier fringes of extension were applied to portray the abrupt transition near the interface. Clearly, the fringe gradient $\Delta N_y/\Delta y$ is negative in the brass and positive in the steel. Strains were extracted, and since the elastic constants were known, stresses were calculated. A remarkable condition was found near the interface, namely a peak compressive stress in the brass and a peak tensile stress in the steel. Subsequent analysis by microscopic moiré interferometry documented a severe stress gradient in the 50 μm zone surrounding the interface. The peak stresses were elastic and the peaks were connected by the severe gradient in the transition zone.

22.2.9 Curved Surfaces

Moiré interferometry has been developed for routine analysis of flat surfaces. However, certain accommodations can be made for curved surfaces when the problem is important enough to invest extra effort. The most straightforward approach is to treat any local region as a flat surface. A small grating mold (cut from a larger mold) could be used to replicate the grating on the curved surface of the specimen. Other innovative techniques can be employed for cylindrical surfaces, or other developable surfaces.

Results shown in Fig. 22.15 are from an important investigation. It is from a study of the ply-by-ply deformation at a central hole in multi-ply composite plates [22.11]. The specimens were thick laminated composite plates, each with a 25.4 mm diameter central hole. The grating was applied to the cylindrical surface of the hole and successive replicas of the deformed grating were made with the specimen at different tensile load levels. First, a cross-line grating was formed on the cylindrical surface of a disk and it was used as a mold to apply the grating to the specimen. Then, with the specimen under load, the deformed grating was replicated (or copied) on another disk. The replica was inserted in a moiré interferometer and deformation data were recorded by a moiré interferometer as a series of narrow strips, each approximating a flat surface. Figure 22.15 shows a mosaic of such strips for a 90° portion of the hole in a cross-ply $[0_4/90_4]_{3S}$ laminate of IM7/5250-4 (graphite fibers in a bismalimide-cyanate ester matrix). An enlarged view of the N_θ fringe pattern at the $\theta = 75°$ location is shown in Fig. 22.15d, together with a graph of the ply-by-ply distribution of shear strains. This is the location of greatest fringe density, and yet the data are revealed with excellent fidelity, enabling dependable determination of strain distributions. The interlaminar shear strains at the 0/90 interfaces are about five times greater than the tensile strain at $\theta = 90°$. A primary purpose of the work was to provide experimental data for the evaluation of computational techniques for composite structures.

22.2.10 Data Enhancement/Phase Stepping

An abundance of load-induced fringes is typical for most applications, sufficient for reliable analyses. For small specimens, however, or within a small field of view for larger specimens, the displacement accumulated across the field will be small (even if the strains are not small); then, the number of fringes is not sufficient and additional data are desired.

Phase stepping, also called fringe shifting, provides additional data. Referring to Fig. 22.9, we recall that the fringe pattern is a contour map of the separation S of

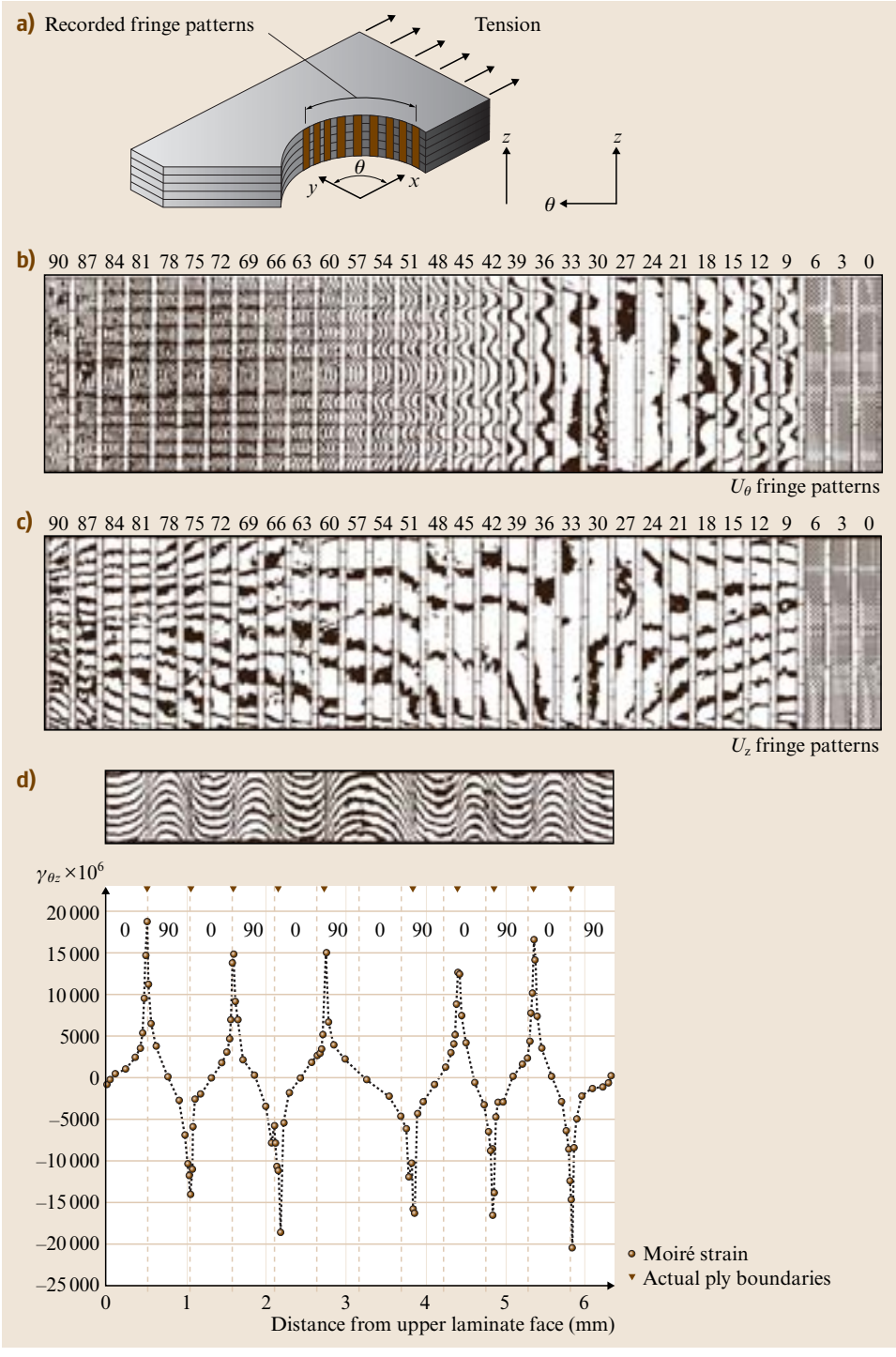

Fig. 22.15a–d Ply-by-ply displacements at the cylindrical surface of a hole in a cross-ply composite plate. **(d)** shows an enlarged view of the U_θ pattern at the 75° location, and the shear strains at that location. (Courtesy of D. H. Mollenhauer)

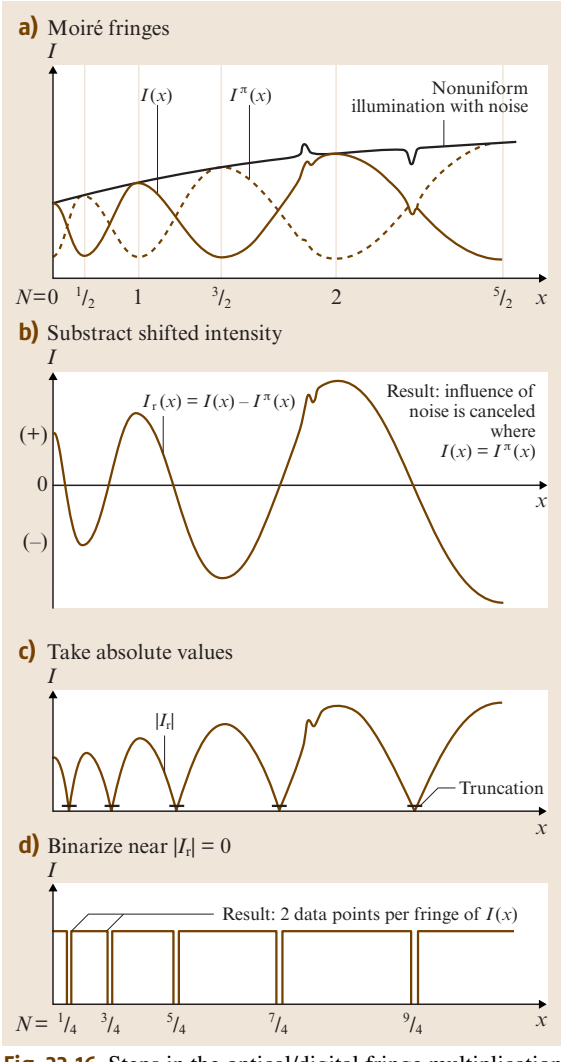

Fig. 22.16 Steps in the optical/digital fringe multiplication (O/DFM) algorithm

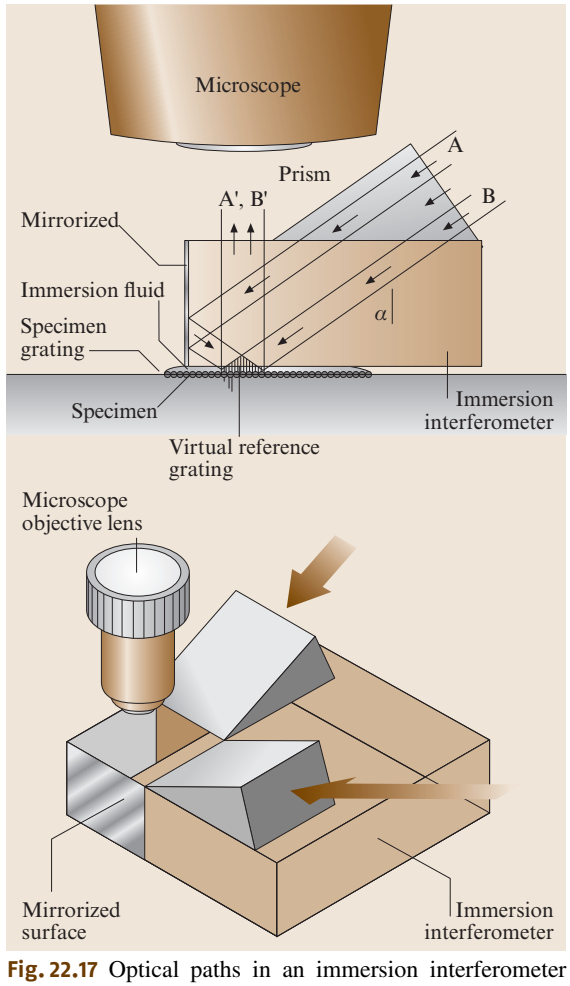

Fig. 22.17 Optical paths in an immersion interferometer and arrangement for U and V fields

wave fronts that emerge from the specimen. In phase stepping, the separation S is increased (or decreased) by a fraction of a wavelength, uniformly across the field. The result is a uniform change of fringe order throughout the field of view; the intensity at every pixel, as measured by the digital camera, is changed. Usually, the phase change is accomplished by translating a mirror, or other optical element in the moiré interferometer, using a piezo-electric actuator to displace the element by a tiny increment. For an achromatic system like that of Fig. 22.7, the phase change can be executed by in-plane translation of the compensator grating.

A common procedure for full-field data enhancement is the quasi-heterodyne method [22.12, 13]. In the simplest implementation, three shifted images of the fringe pattern are recorded, with phase steps of 0, $2\pi/3$ and $4\pi/3$ (fringe shifts of 0, 1/3 and 2/3 of a fringe order). The CCD camera, frame grabber and computer gather the data from the three images, recording the intensity at each pixel as I_1, I_2, I_3. With these data, the quasi-heterodyne algorithm calculates the fractional part of the fringe order N' at each pixel by

$$N' = \frac{1}{2\pi} \arctan \frac{\sqrt{3}\,(I_2 - I_3)}{2I_1 - I_2 - I_3}. \qquad (22.9)$$

Then the fringe order of each pixel is determined by an unwrapping algorithm, whereby neighboring pix-

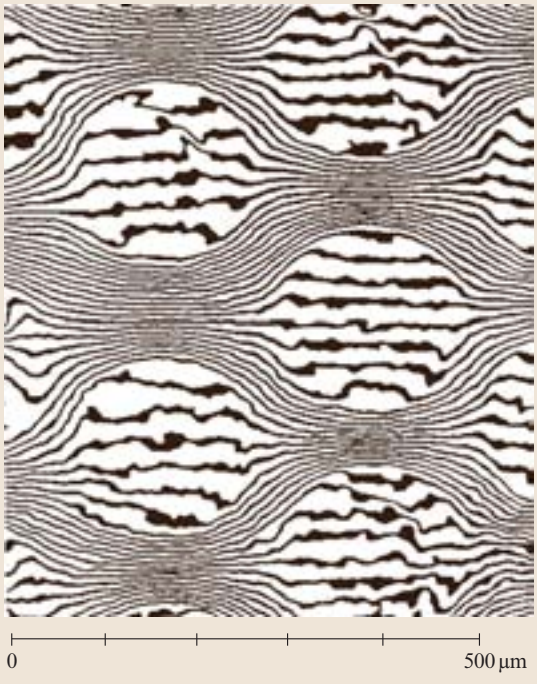

Fig. 22.18 Boron/aluminium composite subjected to a change of temperature of 110 °C. Microscopic moiré interferometry was used with $f = 4800$ lines/mm and $\beta = 6$; 35 nm/contour

els are compared to determine whether an integral fringe order should be added (or subtracted) to the fractional part. Thus, fringe orders are established throughout the field of view. Various other implementations of the quasi-heterodyne method provide flexibility and redundancy by using more than three phase steps.

A lesser known algorithm, called the optical/digital fringe multiplication (O/DFM) method, has also been used for moiré interferometry [22.4]. It shares numerous features with the quasi-heterodyne method, including insensitivity to nonuniform illumination and optical noise. It offers a unique feature, however, because the data that is used comes exclusively from the points in the fringe pattern where the intensity is changing most rapidly. Compared to data taken at (or near) the maximum and minimum intensity points in the fringe pattern, the phase increment per grey level of the CCD camera is many times smaller (approx. 1 : 50), so the data of greatest accuracy is used exclusively.

The algorithm is portrayed in Fig. 22.16 for multiplication by 2. Two fringe patterns are used, patterns stepped by 0 and by π (i. e., two complementary patterns). Their intensities at each pixel are subtracted, truncated and binarized. The result is a contour map of the fringe orders, with two contours per fringe. Multiplication by 4 is obtained using data stepped by 0, $\pi/2$, π and $3\pi/2$. Multiplication by β requires β stepped fringe patterns. Multiplication by $\beta = 12$ has been demonstrated.

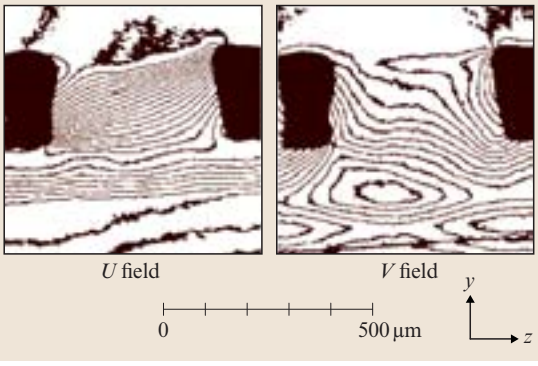

Fig. 22.19 Microscopic moiré fringe contours for a solder ball interconnection in an electronic package. $\Delta T = 60$ °C; $f = 4800$ lines/mm; $\beta = 4$; 52 nm/contour

22.2.11 Microscopic Moiré Interferometry

Within a tiny field of view, the relative displacements are small and few fringes appear across the field. Increased sensitivity is desired. Two techniques have been implemented to progressively increase the number of load-induced fringes. The basic sensitivity is increased by a factor of two by means of an immersion interferometer, and then phase-stepping and the O/DFM algorithm are used to produce a suitably dense fringe pattern.

Figure 22.17 illustrates an immersion interferometer [22.4]; many alternative designs are possible. This one was implemented, with $\lambda = 514$ nm (in air), $\alpha = 54.3°$ and $n = 1.52$ (where n is the index of refraction of the interferometer block). Within the refractive medium the wavelength was reduced to 338 nm, providing a virtual reference grating frequency of 4800 lines/mm. This is twice the frequency used (without immersion) for most macroscopic applications, and it exceeded the theoretical limit for virtual reference gratings produced in air. By (22.3), twice as many fringes are obtained for a given displacement, compared to designs without immersion. For phase stepping, the element labeled *immersion interferometer* is moved lat-

erally by a piezoelectric actuator. Movement of $1/f$ causes a phase change of 2π, so β steps of $1/\beta f$ each are used to implement the fringe multiplication.

Figure 22.18 is an example. The specimen was a unidirectional boron/aluminium composite subjected to thermal loading. The bithermal method was used, where ΔT was 110 °C. Here, $f = 4800$ lines/mm; $\beta = 6$; and the contour interval is 35 nm per contour. The pattern shows the combined effects of thermal strains plus free thermal expansion ($\alpha\Delta T$). When the uniform $\alpha\Delta T$ is subtracted off for each material, the substantial range of stress-induced strains in the aluminium matrix becomes evident.

Figure 22.19 is an example from electronic packaging, showing the displacement fields for a single solder interconnect. Here, $\Delta T = 60$ °C; $f = 4800$ lines/mm; $\beta = 4$; and the contour interval is 52 nm/contour. Details of the small deformation are clearly documented.

22.3 Challenges

The authors visualize two developments that would be important contributions to the experimental mechanics community. We propose that members of the community, worldwide, start modest endeavors to develop these capabilities. The first would enhance the ease and accuracy of strain determinations. The second would further enhance the versatility of moiré interferometry.

22.3.1 Strain Analysis

For most macromechanics analyses, moiré interferometry provides a great number of stress-induced fringes, sufficient for a detailed analysis. Yet, in current practice, there is a tendency to use phase-stepping schemes to reduce these data to graphs of displacements and strain distributions. The phase-stepping algorithms enjoy popularity mostly because they enable automatic data reduction. However, there are many pitfalls. Automated analyses do not recognize extraneous input like those from scratches or other imperfections of the specimen grating. Automated analyses do not cope well with rapidly changing displacement fields, for example, those that can be encountered in composite structures; particularly, automated analyses must not be allowed to extend across regions of dissimilar materials.

Thus, for the majority of applications, interactive schemes should be developed in which the investigator controls the process and makes the decisions. The moiré pattern is itself a map of deformation. The investigator should choose the regions of interest – usually the regions where the fringes are closest together and strains are highest. Techniques should be developed to extract these strains with the highest accuracy. The investigator should deal with possible imperfections in the fringe patterns. He/she should decide whether carrier fringes would aid the analysis.

The authors have proposed ideas on methods to explore and perfect. The challenge is published by the Society for Experimental Mechanics in *Experimental Techniques* [22.14], where the worldwide community is invited to participate. The objective is to devise and share a superior technique for extracting strains, and in an on-going evolution to improve and refine the technique into an easy, accurate and efficient algorithm. The Society will maintain an open website to share the contributions and make them available to everyone.

22.3.2 Replication of Deformed Gratings

In a classical paper by *McKelvie* and *Walker* [22.15], replication was advocated for remote sites and harsh environments, followed by analysis of the replicas in the laboratory. Now, replication is envisioned as a routine practice. In this practice, a grating is applied to the specimen or workpiece in the usual way. Then, the workpiece is subjected to its working loads, for example in a mechanical testing machine, which deforms the specimen and the specimen grating. Replicas of the deformed grating are made at desired intervals in the loading process, and subsequently the replicas are analyzed in a moiré interferometer.

Replication provides numerous advantages for typical applications. No limits are applied to the size of the workpiece. Familiar equipment can be used for loading, including large or special purpose machines. Vibrations and air currents become inconsequential. The technique can be applied in the field, far from the laboratory, and in difficult environments. In many applications, replicas can be made for cases where the loading is not mechanical, but stems from changes of temperature, humidity, chemical or radiation environments, etc.

The replicas can be made on transparent substrates, enabling use of transmission systems of moiré interferometry instead of the current reflection systems. When transmission systems are used, the camera lens can be located very close to the replica and, therefore, high magnifications and high spatial resolution become convenient. Additionally, the replicas become permanent records of the deformation, so there is easy recourse to checking and extending an analysis after an initial investigation.

Thus, replication is extremely attractive for routine use as well as special applications. What developments are required? Although the replication method can be practiced with current technology (Fig. 22.15 is a compelling example) it would be advantageous to find materials and techniques for quick and routine replication of deformed gratings. We believe these techniques will be optimized and broadly implemented; the experimental mechanics community is invited and encouraged to participate in their development.

22.4 Characterization of Moiré Interferometry

The preceding description and examples lead to these conclusions. Moiré interferometry combines the simplicity of geometrical moiré with the high sensitivity of optical interferometry. It measures in-plane displacements with very high sensitivity. Because of the great abundance of displacement data, reliable strain distributions – normal strains and shear strains – can be extracted from the patterns. With knowledge of the material properties, local and global stresses can be determined.

Moiré interferometry is characterized by a list of excellent qualities, including these:

- full-field technique – quantitative measurements can be made throughout the field
- high sensitivity to in-plane displacements U and V – typically 0.417 μm per fringe order, but extended into the nanometer range by microscopic moiré interferometry
- insensitive to out-of-plane displacements W – out-of-plane deformation does not affect the accuracy of in-plane displacement measurements
- high spatial resolution – measurements can be made in tiny zones
- high contrast – the fringe patterns have excellent visibility
- large dynamic range – the method is compatible with large and small displacements, large and small strains, and large and small strain gradients; there are no correlation requirements
- shear strains are determined as accurately as normal strains
- real-time technique – the displacement fields can be viewed as the loads are applied.

Moiré interferometry differs from classical interferometry and holographic interferometry, which are most effective for measuring out-of-plane displacements. It is distinguished from the various methods of speckle interferometry for measuring in-plane displacements, which cannot exhibit the fringe visibility and extensive dynamic range of moiré interferometry. Moiré interferometry has a proven record of applications in engineering and science.

Bibliography

- Comprehensive treatment of moiré interferometry for strain and stress analysis; theory, practice and applications: [22.4] Note: Excerpts are included in this chapter with the kind permission of Springer-Verlag, Berlin, New York.
- Background literature on moiré phenomena; mathematical treatments; not directed to strain analysis: [22.16–18]
- Review article; historic references until 1980s: [22.19]

22.5 Moiré Interferometry in the Microelectronics Industry

Diverse applications from the microelectronics industry are exhibited in this section. However, the studies are not presented in detail; the cited references provide the details. Instead, the raw data are emphasized, that is, the moiré fringe patterns that provide the wealth of information to be extracted from each experiment. The main objective of this Appendix is to illustrate the high quality of the fringe patterns. Note that the patterns can be enlarged on the enclosed DVD – e.g., 200–500% – to evaluate their quality more fully. Of course, when

the raw data are clear and dependable, the experimental results are reliable!

These fringe patterns are contour maps of the deformation caused by changes of temperature and/or moisture content. They are fully quantitative; fringe orders are readily assigned to every fringe (every contour) and the U or V displacement at each point along that contour is simply proportional to the fringe order. Moiré interferometry provides submicron sensitivity; microscopic moiré interferometry provides sensitivity in the nanometer range. Strains can be extracted, too, inasmuch as strains are determined by the rate of a change of fringe order, e.g., $\Delta N_x/\Delta x$; thus, strains are highest where the fringes are closest together.

Moiré interferometry has become extremely important in the electronics industry for electronic packaging studies. The applications – mostly to evaluate thermal strains, but also for hygroscopic deformation, mechanical loading and material characterization – are introduced at design and development, evaluation, and process control stages. The following experiments illustrate the applications.

22.5.1 Temperature-Dependent Deformation

Figure 22.13 illustrates data from a wire-bond plastic ball grid array (WB-PBGA) package subjected to a thermal cycle; maximum and minimum temperatures were 125 and −40 °C. The thermal deformation is complicated, exacerbated by creep and relaxation of the solder and molding compound. Please refer to [22.8] for analysis and discussion.

Ceramic BGA Package Assembly

The objective of this application was to study the temperature and time dependent thermo-mechanical behavior of a ceramic ball grid array (CBGA) package subjected to an accelerated thermal cycling condition. The assembly was a 25 mm CBGA package with 361 I/O's (19 × 19 solder interconnection array) on an FR-4 PCB. A specimen with a strip array configuration was prepared from the assembly, containing five central rows of solder interconnection. The solder interconnection of the package assembly consisted of a high melting point solder ball (90%Pb/10%Sn) and a lower melting point eutectic solder fillet (63%Pb/37%Sn), as illustrated by the insert in Fig. 22.20. The high melting point solder ball does not reflow during the assembly process, so it provides a consistent and reproducible standoff between the ceramic package and the PCB.

Figure 22.20 shows the temperature profile used in the thermal cycle. To ensure a uniform temperature distribution, the specimen was kept at each target temperature for 5 minutes before measurement. The U and V fringe patterns with fringe orders N_x and N_y, respectively, were recorded at each of the lettered temperature levels.

Representative patterns at 55 °C (point B) are shown in Fig. 22.20. The dominant mode of deformation of the solder interconnection is shear, which is caused by the mismatch of the CTE of the ceramic module and the PCB. Consequently, the shear strains at the interconnection increase as *the distance from the neutral point* (DNP) increases, so the last solder ball experiences the highest shear; the second insert in Fig. 22.20 shows the fringes in a magnified view of this interconnection. Note that the fringe orders are marked on the fringe patterns. At the top of the rightmost interconnection, $N_x = 2.5$ is counted along the upper section, starting from the $N_x = 0$ fringe; similarly $N_x = 9.5$ is counted along the lower section of the assembly. In the same way, the fringe orders at the top and bottom of the interconnection can be determined from patterns recorded at each temperature level.

This solder interconnection was analyzed to investigate the effect of the two solder materials. The development of inelastic strains in the solder joints during the thermal cycle is seen in Fig. 22.21, where the horizontal displacements along the vertical centerline are plotted for various stages in the thermal cycle.

It is important to note that the reflow process produced a thin eutectic solder bench between the solder ball and the copper pad, while there was essentially no gap between the solder ball and the ceramic module. Consequently, the shear deformation of the top eutectic fillet was constrained by the solder ball, but the bottom eutectic fillet was free to deform in shear. This sequence of fringe patterns shows that plastic deformation occurred at the higher temperatures. It was concentrated in the eutectic (lower melting point) solder, and this irreversible strain was present in all the subsequent patterns.

Although the fringe patterns from the full specimen were recorded at each temperature level, the region isolated in this series was less than 1 mm^2. Information from the large specimen was needed to establish fringe orders in the tiny interconnection. It is a remarkable feature of moiré interferometry that such detailed local results could be discerned even when the image magnification was low enough to view the full speci-

men. Please refer to [22.9] for analysis of the data and discussion of the results.

22.5.2 Hygroscopic Deformation

Plastic encapsulated microcircuits are used extensively. In spite of many advantages over hermetic packages in terms of size, weight, performance, and cost, an important disadvantage is that the polymeric mold compound absorbs moisture when exposed to a humid environment. Hygroscopic stresses arise when the mold compound and other polymeric materials swell upon absorbing moisture while the adjacent non-polymeric materials, such as the lead frame, die paddle, and silicon chip, do not experience swelling. The differential swelling leads to hygroscopic mismatch stresses in the

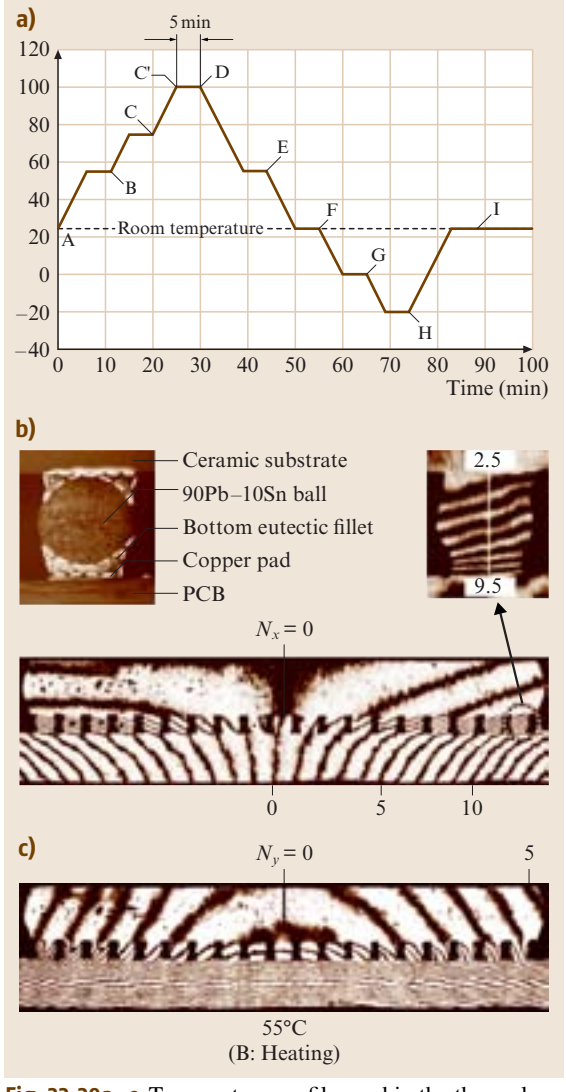

Fig. 22.20a–c Temperature profile used in the thermal cycle (**a**); views of the rightmost solder interconnection (**b**); and horizontal and (**c**) vertical displacement fields of the assembly at 55 °C (point *B*), $f = 2400$ lines/mm

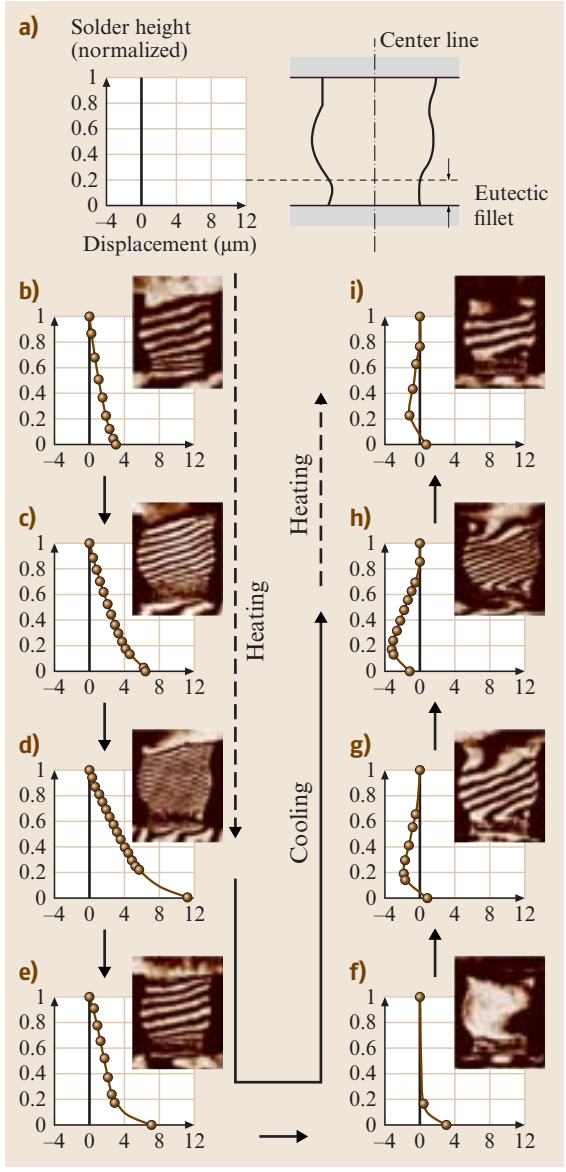

Fig. 22.21 *U* field fringe patterns of the rightmost solder interconnection and the corresponding horizontal displacements determined along the vertical centerline

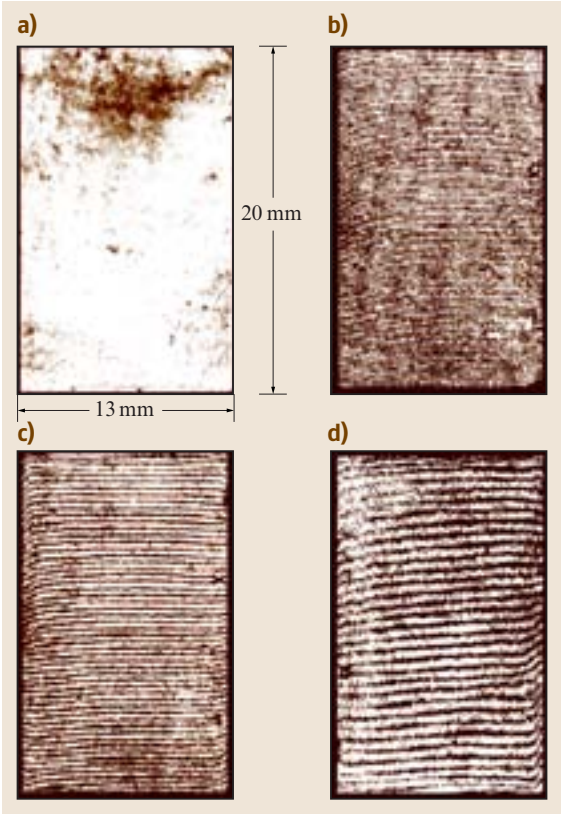

Fig. 22.22a–d V field moiré patterns obtained from a mold compound at 85 °C. **(a)** Null field for the reference sample; **(b)** fringe patterns of the test sample at time intervals of zero, **(c)** 16 h, and **(d)** 400 h, $f = 2400$ lines/mm

package. Moiré interferometry is used effectively to analyze both hygroscopic and thermal deformations.

Coefficient of Hygroscopic Swelling

Figure 22.22 is taken from a series of tests to determine the coefficient of hygroscopic swelling (CHS) of a specific mold compound [22.20]. CHS measurements are made at an elevated temperature of 85 °C. Two equal specimens were used in the test; one was a reference specimen, kept at 85 °C and zero moisture content. The other begins the test at 85 °C and moisture saturation; fringe patterns were recorded as moisture was desorbed as a function of time. Long time intervals were employed, as noted in Fig. 22.22, where the data extends from zero to 400 h. Moisture content was determined at every interval by weighing the specimen.

Figure 22.23 shows the results for three nominally equal samples, where a linear relationship is documented for longitudinal strain versus moisture content.

Hygroscopic Stress in a Plastic Quad Flat Package (PQFP)

Hygroscopic mismatch stresses are documented in [22.21]. The package and the specimen are illustrated in Fig. 22.24. The specimen was conditioned to zero moisture content and the bithermal loading method was used to record the patterns of Fig. 22.25. Figure 22.25a shows the starting condition – the null field representing the specimen at 85 °C and zero moisture. Figure 22.25b shows the patterns for 25 °C and zero moisture. Thus, the deformation incurred by thermal stress alone is depicted here.

Subsequently, the specimen was brought to its moisture saturation level. Figure 22.26 shows the deformation at 85 °C for moisture saturation and for moisture desorption after 8 h. These represent deformation from moisture change alone.

Reliability analyses must include predictive capabilities of hygroscopic swelling as well as thermal deformation. The analysis and discussion in [22.21] shows that hygroscopic strains can exceed thermal strains, thus reflecting the importance of both.

22.5.3 Standard Qualification Test of Optoelectronics Package

Long-haul telecommunication systems are powered by high-performance semiconductor lasers. The light, generated by a laser chip, is coupled into an optical fiber using a system of lenses. The laser temperature is con-

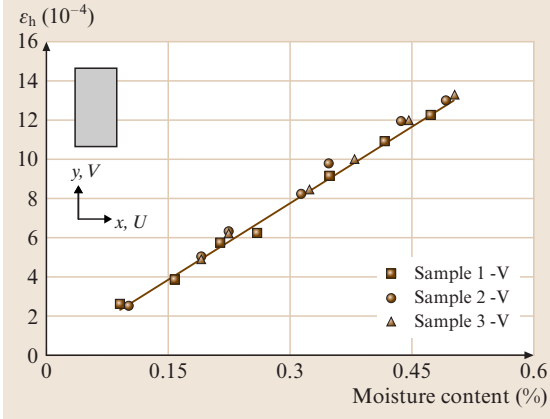

Fig. 22.23 Hygroscopic strain versus moisture content obtained from the moiré fringes

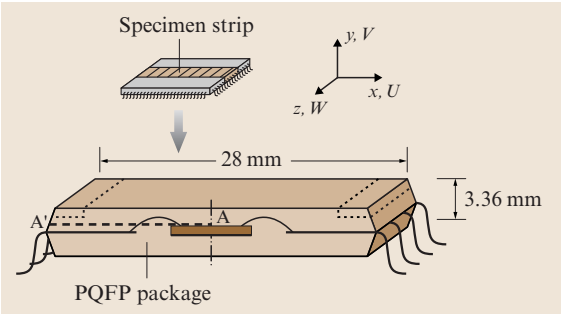

Fig. 22.24 PQFP package for moiré experiments

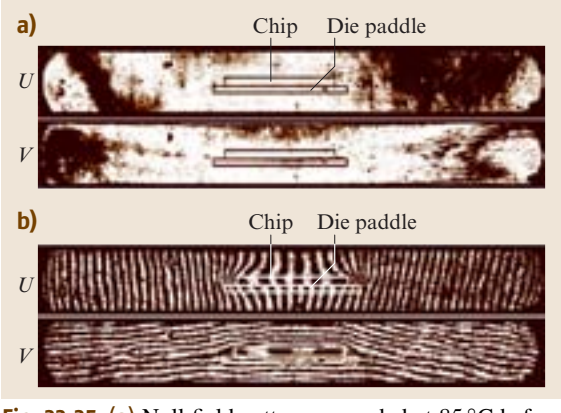

Fig. 22.25 **(a)** Null field patterns recorded at 85 °C before moisture absorption, and **(b)** fringe patterns after cooling the package to 25 °C ($\Delta T = 60$ °C, zero moisture), $f =$ 2400 lines/mm

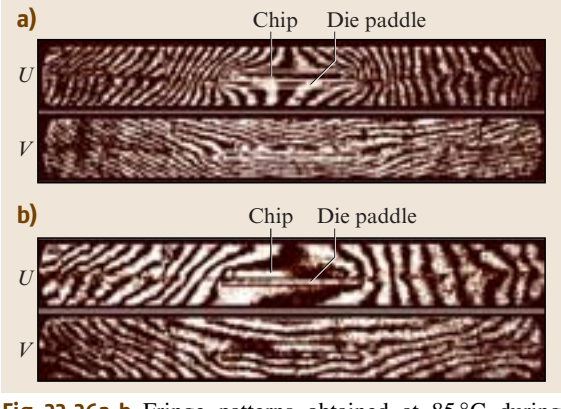

Fig. 22.26a,b Fringe patterns obtained at 85 °C during desorption process **(a)** at moisture saturation and **(b)** after 8 h at 85 °C, $f = 2400$ lines/mm

trolled by a thermoelectric cooler (TEC) in order to produce a constant wavelength. Figure 22.27 shows a generic package. The package body and the base are joined by brazing. The lenses and fiber are fixed in place

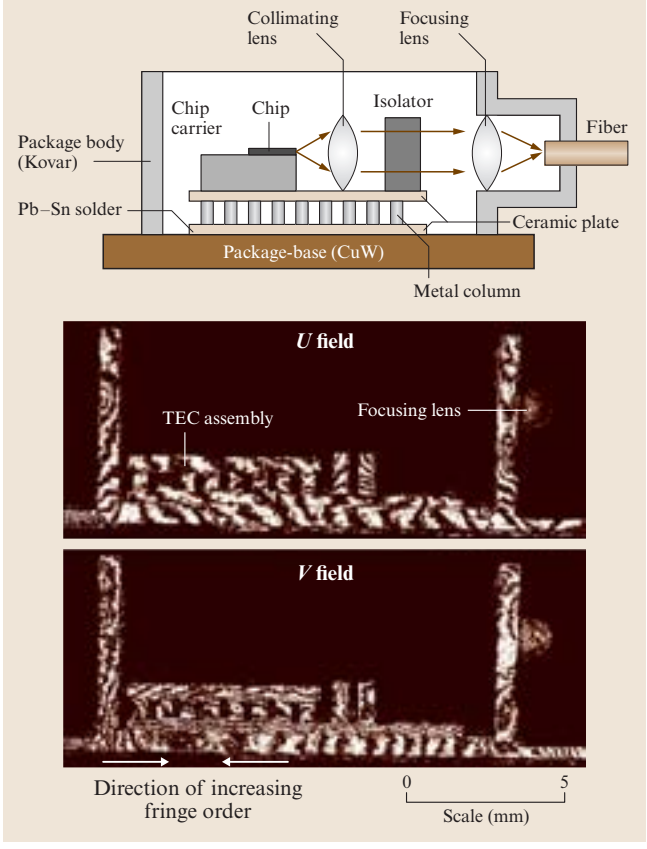

Fig. 22.27 Schematic illustration of a generic optoelectronics package, and the U and V patterns caused by the high-temperature-storage (HTS) test. Note: the fringes are multiplied by O/DFM by a factor of $\beta = 4$; $f = 2400$ lines/mm; the contour interval is 0.104 μm/fringe

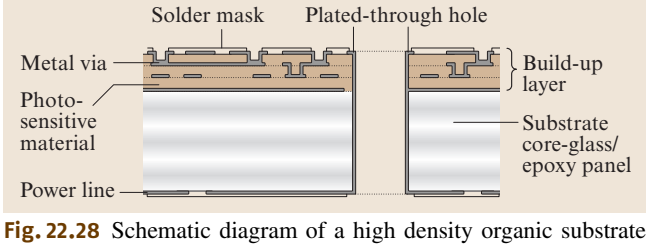

Fig. 22.28 Schematic diagram of a high density organic substrate with build-up structures

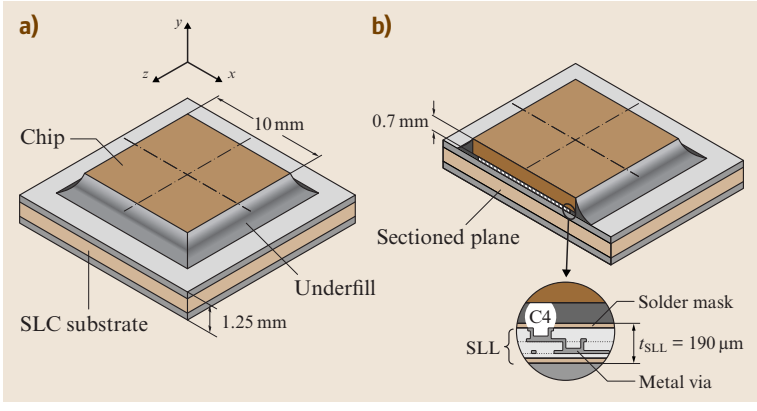

Fig. 22.29a,b Schematic diagram of the flip-chip assembly on a high-density substrate **(a)** before and **(b)** after specimen preparation

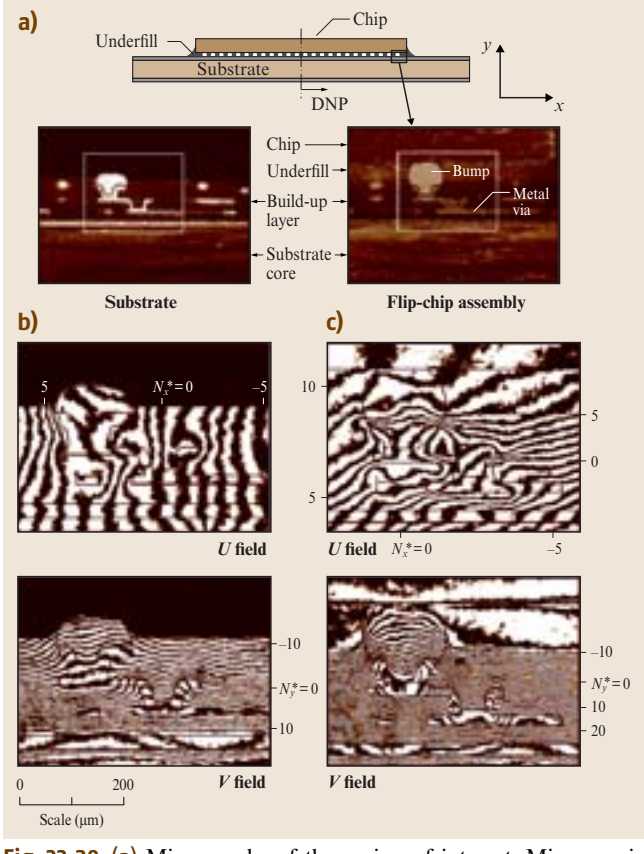

Fig. 22.30 **(a)** Micrographs of the region of interest. Microscopic U and V displacement fields of **(b)** bare substrate and **(c)** flip-chip assembly, $\Delta T = -70\,^{\circ}\mathrm{C}$; $f = 4800$ lines/mm; $\beta = 4$; the contour interval is 52 nm/fringe

by various means, like solder, epoxy and laser welding. Thus, the assembly is a complex system that consists of many materials with different thermal coefficients of expansion, joined by a hierarchy of attachment methods.

The spot-size of the light focused at the fiber is approximately equal to the diameter of the fiber-core, typically 8 µm. Tiny displacements of any optical component are sufficient to shift the focused light spot away from the fiber core and induce a serious loss of coupling efficiency. Accordingly, characterization of the structural behavior is crucial to ensure a stable optical power output.

An experimental investigation of the global deformation of the package-TEC assembly was conducted using moiré interferometry. The package-TEC assembly was cut to expose its cross-section, yet preserve the three-dimensional integrity of the assembly. The cross-section was ground flat and a specimen grating was replicated at room temperature. The interferometer was adjusted with the specimen to provide null fringe patterns in the U and V fields. This adjustment was preserved while the package assembly was subjected to the standard high-temperature-storage (HTS) test condition (85 °C for 100 h). Then, the specimen was cooled to room temperature and the U and V fields were recorded. The resultant fringe patterns after 100 h of HTS are shown in Fig. 22.27, where the fringes were multiplied by the O/DFM method. The fringe multiplication factor was 4, and the resultant contour interval was 0.104 µm per fringe. The fringes document the deformation of the assembly after the HTS.

The results show bending in the base and the attached TEC. These two dissimilar materials were joined by soldering at elevated temperature; when they cooled to room temperature, thermal stresses developed in the solder. Subsequently, the thermal stresses relaxed during the HTS test, resulting in the bending seen in the figure.

The above observation provides important guidelines to the placement of the laser chip and collimating lens mounted on the TEC. It is clear that they should be located toward the front of the TEC or closer to the focusing lens. Otherwise, the change in deformation would lead to a change in angle of the light beam, causing a loss of optical power coupled into the fiber [22.22].

22.5.4 Micromechanics Studies by Microscopic Moiré Interferometry

Micro Via in Build-Up Structure

One of several purposes of a chip carrier, or substrate, is to provide conducting paths between the extremely compact circuits on the chip and the more widely spaced terminals on the PCB. Recent micro via technology enables the industry to produce laminate substrates with imbedded conductors of high density and fine pitch, as required for advanced assemblies. A cross-sectional view of a high-density organic substrate is illustrated in Fig. 22.28. To produce the substrate, photosensitive dielectric layers (insulators) are built up sequentially, with each layer containing a patterned film of copper plating, typically 25 μm thick, to form the imbedded conductors.

In subsequent operations, solder bumps connect the active chip to the substrate, and an underfill adhesive is used to fill the air space between the chip and substrate. Microscopic moiré interferometry was employed to quantify the effect of the underfill on the deformation of the microstructures within the build-up layers. Two specimen configurations were analyzed: a bare substrate and a flip-chip package. The flip-chip assembly is illustrated schematically in Fig. 22.29a with its relevant dimensions.

The specimens were cut and ground to expose the desired microstructures as illustrated schematically in Fig. 22.29b, where the insert depicts the detailed microstructures of interest. An epoxy specimen grating was applied at an elevated temperature of 92 °C in a small region containing the microstructures. The fringes were recorded at a room temperature of 22 °C, capturing the thermal deformation incurred by $\Delta T = -70\,^{\circ}\mathrm{C}$.

The critical region studied here is marked by a dashed box in Fig. 22.30a; it is approximately 500 μm by 375 μm. The resultant fringe patterns are shown in Fig. 22.30 for the bare substrate and the flip-chip assembly.

The moiré interferometer produced a virtual reference grating of 4800 lines/mm; the O/DFM method was used to provide a fringe multiplication factor of $\beta = 4$. Thus, the contour interval in Fig. 22.30 is 52 nm/fringe order. Fringe orders are marked in the figure.

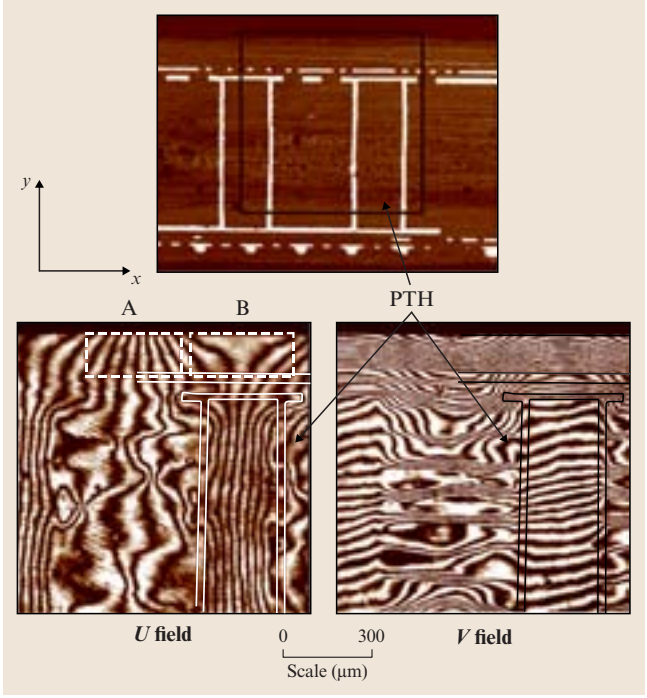

Fig. 22.31 Cross-sectional view of substrate with plated-through-holes; contour maps of the U and V displacement fields for $\Delta T = -80\,^{\circ}\mathrm{C}$, $f = 4800$ lines/mm; $\beta = 2$; the contour interval is 104 nm/fringe (Courtesy S. Cho, Intel)

These contour maps of the U and V displacement fields show a remarkable wealth of detail. The contours are unambiguous, clearly defined, readily analyzed. Again, the reader should increase the magnification of the image to gain further appreciation of its clarity. Please see [22.23] for analysis and discussion.

Local CTE Variations in High Performance Substrate

A high performance substrate accommodates various electrical components such as CPU, capacitors, resisters, etc. The substrate is a complex composite system, which includes layers of epoxy, woven fiberglass, and copper planes.

For reliability assessment of 1st level interconnects, the global CTE mismatch between the silicon chip (≈ 3 ppm/°C) and the substrate (≈ 17 ppm/°C), and also the local CTE variations, must be considered. Microscopic moiré interferometry was employed

to determine the local CTE variations around two plated-through-holes (PTH). Figure 22.31 shows the microscopic U and V displacement fields of the PTH area, induced by ΔT of $-80\,^{\circ}\mathrm{C}$, where the contour interval is 104 nm/fringe.

The fringe patterns clearly show the homogenous nature of the plug material inside the PTH, indicated by the uniformly spaced U and V fringes, and the heterogeneous nature of fiber/resin laminated areas located between the PTHs. For the regions marked as A and B in Fig. 22.31, the effective CTE on the upper surface differ by 8 times in the U field (33.7 and 4.0 ppm/°C). This resulted from variations of materials and features comprising the substrate. The local fluctuations of CTE around these features are the critical information needed to identify areas of failure risk within the substrate.

Again, please view the patterns at increased magnification, and refer to [22.22] for additional information.

References

22.1 C.A. Walker: A historical review of moiré interferometry, Exp. Mech. **34**(4), 281–299 (1994)

22.2 E.M. Weissman, D. Post: Moiré interferometry near the theoretical limit, Appl. Opt. **21**(9), 1621–1623 (1982)

22.3 D. Post: Moiré fringe multiplication with a non-symmetrical doubly-blazed reference grating, Appl. Opt. **10**(4), 901–907 (1971)

22.4 D. Post, B. Han, P.G. Ifju: *High Sensitivity Moiré: Experimental Analysis for Mechanics and Materials Science and Technology* (Springer, Berlin, Heidelberg 1994)

22.5 A.J. Durelli, V.J. Parks: *Moiré Analysis of Strain* (Prentice Hall, Englewood Cliffs 1970)

22.6 Y. Guo, D. Post, R. Czarnek: The magic of carrier fringes in moiré interferometry, Exp. Mech. **29**(2), 169–173 (1989)

22.7 P.G. Ifju, D. Post: *A compact double notched specimen for in-plane shear testing, Proc. SEM Conf. Experimental Mechanics* (Society for Experimental Mechanics, Bethel 1989) pp. 337–342

22.8 S.-M. Cho, S.-Y. Cho, B. Han: Observing real-time thermal deformations in electronic packaging, Exp. Tech. **26**(3), 25 (2002)

22.9 S.-M. Cho, B. Han, J. Joo: Temperature dependent deformation analysis of ball grid array package assembly under accelerated thermal cycling condition, J. Electron. Packaging, Trans. ASME **126**, 41–47 (2004)

22.10 D. Post, J.D. Wood, B. Han, V.J. Parks, F.P. Gerstle Jr.: Thermal stresses in a bimaterial joint: an experimental analysis, ASME J. Appl. Mech. **61**(1), 192–198 (1994)

22.11 D.H. Mollenhauer, K.L. Reifsnider: Interlaminar deformation along the cylindrical surface of a hole in laminated composites – experimental analysis by moiré interferometry, J. Compos. Technol. Res. **23**(3), 177–188 (2001)

22.12 K. Creath: Phase measurement interferometry techniques, Prog. Opt. **26**, 349–393 (1988)

22.13 K. Creath: Temporal phase measurement methods. In: *Interferogram Analysis*, ed. by D.W. Robinson, G.T. Reid (Institute of Physics, London 1993) pp. 94–140

22.14 D. Post: Rapid analysis of moiré fringes, Exp. Techniques **29**(5), 12–14 (2005)

22.15 J. McKelvie, C.A. Walker: A practical multiplied moiré-fringe technique, Exp. Mech. **18**(8), 316–320 (1978)

22.16 K. Patorski: *Handbook of the Moiré Fringe Technique* (Elsevier, New York 1993)

22.17 O. Kafri, I. Glatt: *The Physics of Moiré Metrology* (Wiley, New York 1990)

22.18 J. Guild: *The Interference Systems of Crossed Diffraction Gratings, Theory of Moiré Fringes* (Oxford Univ. Press, New York 1956)

22.19 C.A. Sciammarella: The moiré method, A review, Exp. Mech. **22**(11), 418–433 (1982)

22.20 E. Stellrecht, B. Han, M. Pecht: Measurement of the hygroscopic swelling coefficient in mold compounds using moiré interferometry, Exp. Techn. **27**(4), 40–44 (2003)

22.21 E. Stellrecht, B. Han, M. Pecht: Characterization of hygroscopic swelling behavior of mold compounds and plastic packages, IEEE Trans. Compon. Packag. Technol. **27**(3), 499–506 (2004)

22.22 B. Han: Characterization of stresses and strains in microelectronic and photonic devices using photomechanics methods. In: *Micro- and Optoelectronic Materials and Structures*, ed. by Y.C. Lee, A. Suhir (Springer, New York 2007)

22.23 B. Han, P. Kunthong: Micro-mechanical deformation analysis of surface laminar circuit in organic flip-chip package: An experimental study, J. Electron. Packag. Trans. ASME **122**(3), 294–300 (2000)

http://www.springer.com/978-0-387-26883-5

Springer Handbook of Experimental Solid Mechanics
Sharpe, Jr., W.N. (Ed.)
2008, XXX, 1098 p., Hardcover
ISBN: 978-0-387-26883-5